ISSN 1331-7210

Engineering Power

BULLETIN OF THE CROATIAN ACADEMY OF ENGINEERING Vol. 15(1) 2020

EDITOR-IN-CHIEF'S WORD

In the 26 years of its existence, the Croatian Academy of Engineering Sciences has always endeavoured to publish the results of its outstanding members in the professional and scientific research fields, whereby an insight into the relevant achievements of engineering sciences in Croatia is given. The guest editor of this issue is Željko Domazet, PhD, a full member of the Croatian Academy of Engineering and Professor at the Faculty of Electrical Engineering, Mechanical Engineering and Naval Architecture, University of Split.

I believe you will read with great interest in this issue about research into fatigue, cracks and failures that affect our professional and personal lives. Ž. Domazet and his colleagues present analyses of failure types and the possibility of repairing cracks and defects, which have been successfully carried out and are presented here.

Editor-in-Chief
Vladimir Andročec, President of the Croatian Academy of Engineering

EDITOR'S WORD

Dear readers,

In this edition of HATZ bulletin Engineering Power we continue to present activities of the research groups on diverse topics, conducted by members of the Academy from different Croatian universities.

The Guest-Editor of this issue is Željko Domazet, PhD, Professor at the Faculty of Electrical Engineering, Mechanical Engineering and Naval Architecture, University of Split, and full member of the Academy in the Department of Mechanical Engineering and Naval Architecture.

Editor
Zdravko Terze, Vice-President of the Croatian Academy of Engineering

FOREWORD

In spite of numerous and expensive research in the field of fatigue, cracks and failures caused by fatigue occur every day in all fields of human activity. Such failures typically cause high expenses and danger for human lives.

Perhaps the best definition of fatigue is one of the *ASME Boiler and Pressure Vessel Code* (ASME 2010) which defines fatigue as "… conditions leading to fracture under repeated or fluctuating stresses having a maximum value less than the tensile strength of the material." Fatigue damage in a metal is a progressive, localized, permanent structural change. A fortunate circumstance with many fatigue failures is a relatively long crack propagation period from its origin to the final failure. Due to it a crack can easily be discovered and the corresponding reparation action can be undertaken.

The following papers present some typical fatigue damages in our industry and transport. The complete damage analysis (numerical and/or experimental stress distribution evaluation, fractography, assessment of remaining service life, etc.) showed two facts:

– the design errors caused all of these, as well as many other fatigue cracks and failures,

– the analysis confirmed the possibility of crack and failure repairs, which has been successfully done and presented here.

Guest-Editor
Željko Domazet, University of Split, Faculty of Electrical Engineering, Mechanical Engineering and Naval Architecture

CONTENT

Željko Domazet[1], *Lovre Krstulović-Opara*[1], *Francisko Lukša*[1]

Fatigue Failures in Industry and Their Repairs – Case Studies

[1]Faculty of Electrical Engineering, Mechanical Engineering and Naval Architecture, University of Split, Split, Croatia

Abstract

In spite of numerous and expensive researches in the field of fatigue, cracks and failures caused by fatigue occur every day in all fields of human activity. The paper presents some typical fatigue damages in industry and transport. Fatigue failure of the main engine lateral support (at bulk carrier), fatigue cracks on the large portal crane, and fatigue cracks and failures of the large gear wheel of the cement mill are described. The complete fatigue damage analysis and repair procedures are presented, too.

Keywords*: fatigue cracks, fatigue damages, fatigue analysis and repair*

1. Fatigue failures on the main engine lateral supports

Fatigue failures of the main engine lateral supports appeared in series of new bulk carrier ships (38100 DWT, main engine power 7150 kW). These failures caused a significant financial impact to their owner, too. On all of these sister ships, supports cracked after approximately the same period of a few months of use.

1.1 Failure description

A consequence of the cracking of the supports, Fig. 1, is obligatory stopping of the main engine. After that had happened, the crew usually attached additional reinforcements until new supports were finished. Therefore, crack surfaces were not examined and only crack locations were known. The supports were cracked or failed on the location marked in Fig. 1.

Also, it was not known whether the crack started from the middle of the beam and spread towards the edges or vice versa. After cracking one of the supports, loads were probably redistributed, each time in a different manner. According to the description of cracks and failures, it was obviously that fatigue of material took place again, and its causes should be detected by detailed stress analysis.

Fig. 1. Bulk carrier "Don Frane Bulić"

1.2 Stress analysis

Due to the complicated shape of the crack area stress analysis was performed by means of strain gages. Strain gages were installed on all four beams (Fig. 2) in order to obtain operational loads (axial forces and bending moments).

The measurements took place during the sea trial of the new ship from the series. Measurement of local stresses was done at the locations of crack initiation spots, i.e. at the spot of the maximum stresses. As the observed bending moments were negligible, attention was put on the middle

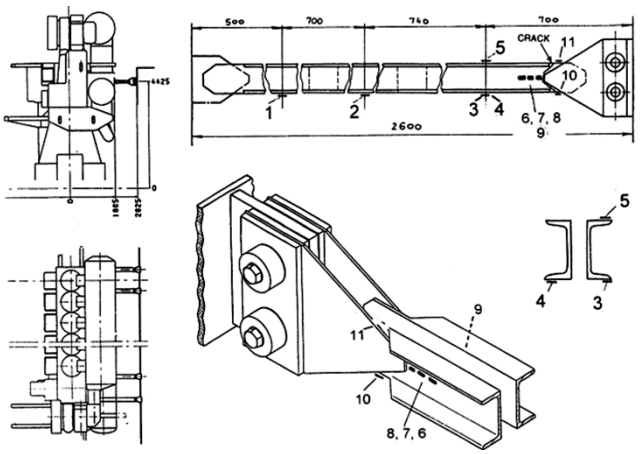

Fig. 2. Lateral engine support with observed failures and setup of the measurements for stress determination

of the joint. In order to obtain maximum stress, three strain gages were applied (15-17), Fig. 2. As all four supports were not manufactured geometrically identically, on the other side of support 3, strain gage 18 was applied as well as gages 21, 22, 23 on supports 1, 2, 4, respectively. A significant difference of the measured axial forces between the supports was detected. One of the beams was loaded with approx. 50% lower load. However, maximum axial force F = 20 kN (calculated from the nominal stresses) was within the range of design load values. Measurements gave no significant bending moments. The results of nominal stresses (σ = 10¸15 MPa) could not be the reason for fatigue cracks, in spite of observed differences from one support to others. Stresses at the crack initiation points were measured to evaluate the quality of design. Three strain gages (15, 16 and 17) were used for extrapolation of maximal stresses. Maximum stresses at the welds toe are extrapolated. Their amplitudes vary depending on the weld design, but the measured values of 70 or even 80 MPa could easily cause the initiation and propagation of fatigue cracks.

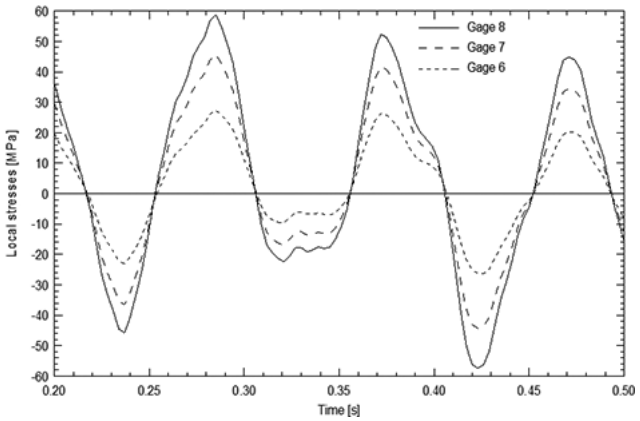

Fig. 3. Local stress determination

1.3 The first case study discussion

According to the existing S-N curves for such weldments and determined maximum stresses, it is possible to predict the fatigue life of approx. 5 x 10 6 cycles, or a few weeks of service. This service life is too short, compared with expected 20 years. This prediction had good agreement with the time to failure observed on the former ships. Failures are mainly caused by the inadequate joint design, the support and ship (hull) structure from one side, and insufficient weld quality. Namely, stress concentration factor in the critical area $\mathbf{s}_{loc}/\mathbf{s}_{nom}$ ~5 was quite unacceptable. It should be not more than 2 – 2.5, and **a** complete reconstruction of this important detail was necessary.

2. Fatigue cracks at large portal crane

This case study presents fatigue damage analysis and repair procedure that was carried out after the cracks at 250 kN portal crane were detected, Fig. 4. After a few years of crane service, fatigue cracks occurred at several critical points – bottom of the tower and both legs of the portal. Previous attempts of repair by simple welding of cracks were not successful, because new cracks were detected soon after the repair. When cracks reached the critical length, the exploitation of the crane was stopped and detailed analysis was carried out.

Fig. 4. Portal crane in Shipyard Split

2.1 Failure description

Cracks occurred at transition areas from vertical to horizontal supports on both legs, growing from the corners and bringing into danger the whole construction, Fig. 4. The first cracks were detected soon after the crane was

placed in the shipyard, so the allowed carrying capacity was reduced from 250 kN to 50 kN, figure 4, but the cracks continued to grow. In order to find the source of crack initiation and growth, the complete documentation and calculations were checked. It was found that calculations were performed by using simple beam elements, without taking into account stress concentration, and influences of inertial forces and wind were underestimated. Those facts led us to perform complete static and fatigue analysis, to measure real stresses during typical manoeuvres and to redesign the critical places of the crane.

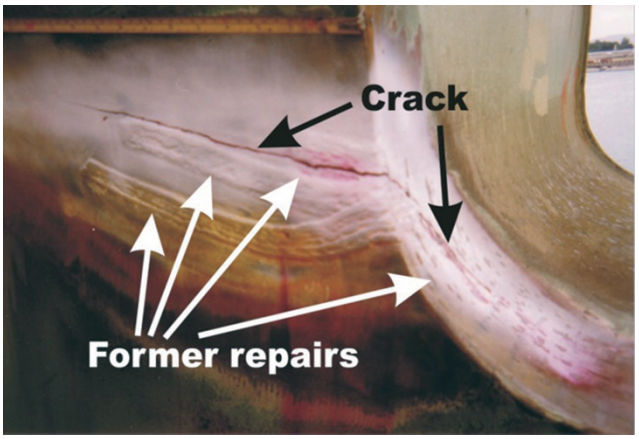

Fig. 5. Detected cracks

2.2 Measurement of stresses, COD and acceleration

To determine the dynamic behaviour of the construction strain gauges, two induction transducers for displacement and capacitive transducer for acceleration were applied. Test load was 50 kN, without wind during the measurement. All data were recorded during the typical working cycles of the crane and results were presented by a great number of diagrams. Based on the analysis of these diagrams, some general conclusions can be set out:

- the highest measure of stress amplitude was about 150 MPa, but in practice stresses can be higher, due to several reasons: – strain gauges were not attached at the places of highest stress concentration (access is not possible because of cracks)
- stress concentration factor ak is about 2, what is not theoretical maximum
- crack opening displacements reached 1.5 mm, what according to the Fracture Mechanics COD – concept indicates the stress of about 200-300 MPa
- measured values of acceleration were up to 0.2 m/s^2, what is acceptable, but during the test the crane was driven very carefully – in every day's use, and under the influence of wind, these values can be higher.

2.3 FEM Analysis

Finite Elements Method was used to determine the global stress distribution and to find out the weak points of the construction. Linear elastic model and 3D- Plate elements with four or three nodes and six degrees of freedom were used. The geometry of the lower part of the crane was defined by 2191 elements (2327 elements in variants with stiffeners). Boundary conditions were defined as follows:

– all six degrees of freedom on the nodes at the bottom contour of model were constrained,
– concentrated forces and bending moments are distributed along the nodes on the top of the model, representing the own weight of the upper part of the crane and particular load case. The complete analysis included 17 variants, with various loads, with or without stiffeners, with different orientation of the crane branch and including the construction weight. The mesh and typical results of FEM analysis are shown in Fig. 6.

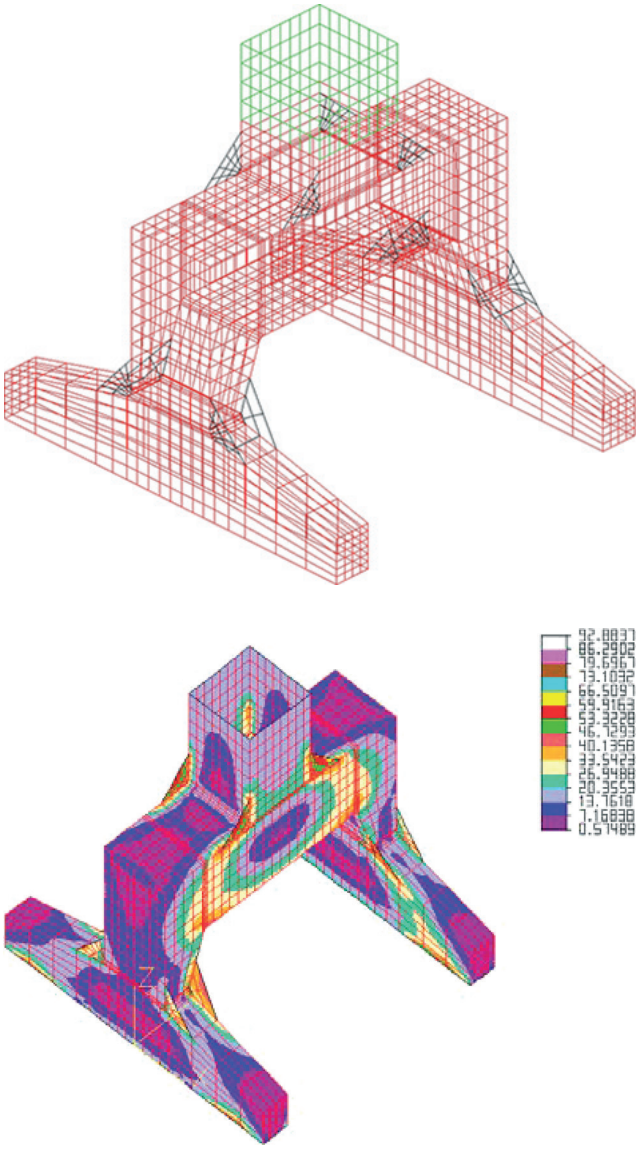

Fig. 6. FEM mesh and some results

2.4 Repair procedure

Strain gauge measurement and FEM analysis showed the source of the crack initiation – high stress concentration in the transition areas from the vertical to horizontal

part of the supports. At critical points those stresses exceeded the fatigue strength of the material and caused the crack initiation and growth. Variable loads cannot be avoided, so the only solution was to redesign the critical areas in order to redistribute local stresses. FEM analysis also showed the best way for redistribution of high stresses: application of triangle stiffeners that fit the existing construction (Fig. 7). Those stiffeners were welded by using the MAG process. Heat treatment was used to minimize residual stresses, and fatigue limit of welds increased by grinding the weld toes and roots. After the repair was completed, stresses at critical points were measured once again and compared to the values predicted by FEM. According to the data obtained from FEM and strain gauges measurements, it is clear that stresses at critical points were significantly lowered, especially in critical areas. All the stresses were under the fatigue limit, so the main source of crack growth was removed.

Fig. 7. Positions of attached strain gauges

2.5 The second case study discussion

The sharp transition from vertical to horizontal plates at the crane leg caused the initiation and growth of fatigue cracks that endangered the whole construction. By replacing the plates with cracks and applying the stiffeners at the places of the crack initiation, the sources of fatigue damages were removed and the maximum stresses at the redesigned construction were lowered to approximately one half of the previous values. Later examinations of the crane construction confirmed the success of this repair – two years after repair no new cracks were detected.

3. Fatigue cracks at cement mill gear

After 20 years in service, the great gear wheel of cement mill, Fig. 7, failed due to fatigue. When the whole mill plant was stopped and inspected, additional seventeen fatigue cracks were found at the tooth fillets. The gear wheel was fabricated of cast steel and mounted in two ring parts at the front side of the cement mill, Fig. 8.

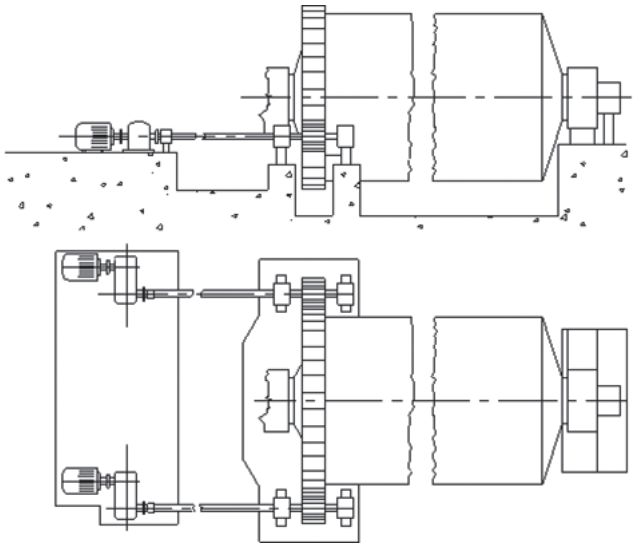

	Large gear	Small gears
Med. diameter	6778 mm	960 mm
Teeth width	600 mm	600 mm
Tooth number	230	32
Module	30 mm	30 mm
Gear rim thick.	80 mm	160 mm
Gear mass	25000 kg	2815 kg

Fig. 8. Cement mill and its characteristics

3.1 Failure description

At several positions, very close to the surface, a lot of casting errors (pores, slag inclusions, etc.) were found, Fig. 8. Joint efforts of alternating stresses, casting errors (sized several millimeters to several centimeters) and most likely existence of residual tensile stresses caused fatigue cracks initiation and propagation at the critical positions. The cross section of the gear rim, where complete fatigue failure occurred (fatigue crack No. 2), was additionally weakened by decreasing the rim thickness due to connecting bolts. The position of the cracks is shown in Fig. 7. The surface crack length varied from 20 mm to 600 mm (total failure). The position and size (surface length) of each discovered crack were estimated by means of non-destructive testing (magneto-flux method). In order to determine the complete data on crack shape and size (depth), and to perform repair welding, voluminous work (cracks removal by arc-air grooving) was undertaken.

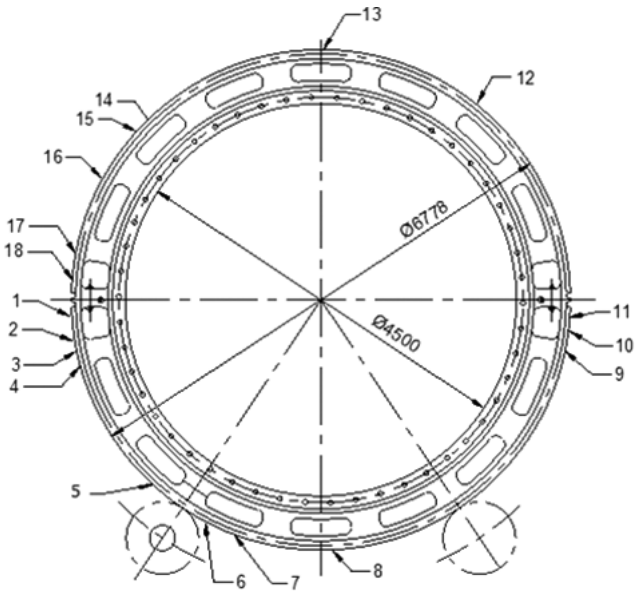

Fatigue crack number	Crack position (teeth number)	Crack surface length (mm)
1	2-3	200
2	3-4	600, failure
3	16-17	290
4	19-20	330
5	24-25	20
6	26-27	315
7	32-33	50
8	63-64	320
9	112-113	250
10	113-114	180
11	114-115	200
12	158-159	100
13	168-169	400
14	209-210	160
15	210-211	60
16	216-217	120
17	229-230	200
18	230-231	90

Fig. 9. Detected cracks on the cement mill

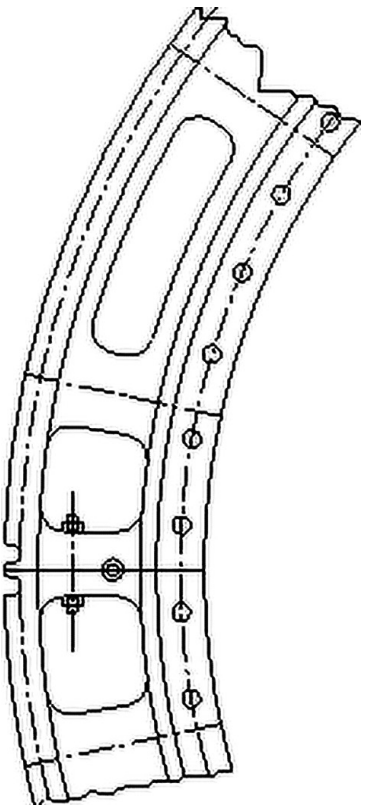

Fig. 10. Additionally weakened gear by decreasing the rim thickness due to connecting bolts (position 2 from Fig. 7)

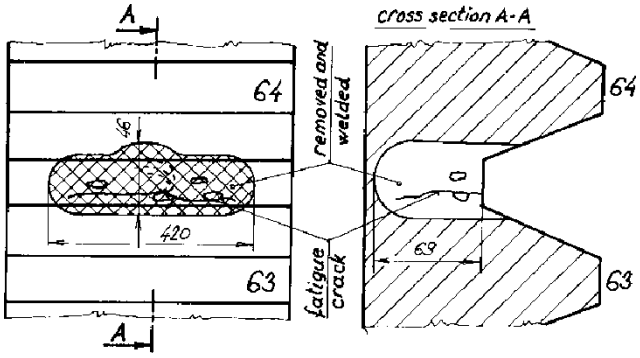

Fig. 11. Typical fatigue crack on the cement mill

3.2 Stress analysis and fatigue cracks repair

During each revolution of the cement mill and large gear, every tooth was loaded twice (two small gears) by tooth force alternating from zero to the maximum value. Numerical method (FEM) was used to determine the stress distribution at the gear rim. Calculated maximum stress amplitudes were found at the tooth fillet, approximately 50 – 115 MPa, depending on their positions on the surface. Stress intensity decreased very fast in the depth of the gear rim.

These stress values could not be the only reason for cracks initiation and propagation. In spite of a great number of cracks and one complete failure of the gear ring, repair welding was performed. All necessary steps for the best quality insurance (best welders, best welding rods, pre-heating, very slow cooling conditions, NDT inspection following every layer, hammering of all layers, etc.) were respected and documented.

All described activities took two months and cost approx. $50 000 instead of $300 000 for a new gear ring and four months for its delivery and assembly. Three years after repair and frequent controls during the service, no further cracks were reported.

4. Conclusion

The case studies presented in this paper illustrate the circumstances of an inappropriate design, from the fatigue point of view. It is obvious that in the case of variable

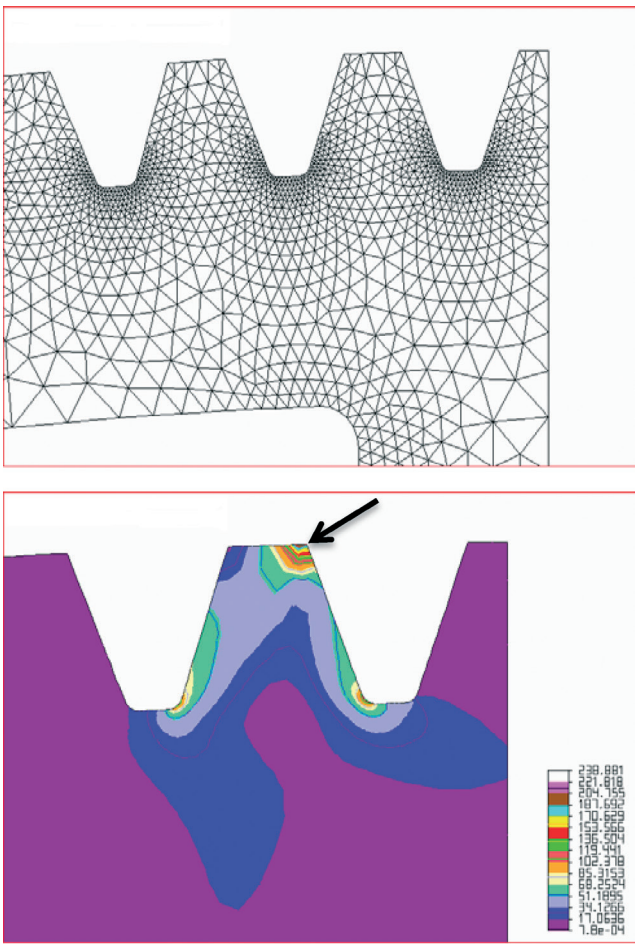

Fig. 12. Stress distribution and stress concentration

Fig. 13. Cracks removal by arc-air grooving before repair welding and subsequent slow cooling

loads, special attention should be paid to fatigue crack avoidance and fatigue crack repairs as well. A lucky circumstance with many fatigue failures is a relatively long crack propagation period from its origin to the final failure and a crack can be detected easily. What to do with detected fatigue cracks is a well-known question in such situations. The usual answer is one of the following actions:

- instantaneous unloading of the entire system and replacing the cracked component
- reducing the external loads and continuing careful crack growth control, and
- retarding, stopping or even eliminating the crack (crack repair) in a very short time.

As the complete replacement can be time consuming and expensive, and the reduction of service loads with existing fatigue crack is very dangerous and mostly unacceptable, fatigue crack repairs seem to be the best solution. The necessary steps for a successful repair of fatigue cracked component should be [Domazet 1996]:

a) Damage analysis: the first step with any damage and its possible repair should be damage analysis. It should give answers to some important questions, such as: what is the reason for the fatigue crack, how dangerous is the existing fatigue crack, how long is the remaining component life, etc.

b) Damage repair: the most frequent fatigue crack repair methods are: repair welding, metal reinforcements, CFRP patches, arrest holes, etc. The final choice of the adequate method and its parameters depend on all data obtained by damage analysis and knowledge of repair methods. The role of experience and case studies from literature should not be avoided either.

c) Reliability of repaired component: reliability of remaining life estimation of repaired components in accordance with new stress distribution and possible improvements of fatigue strength. For this reason, the S-N curve of the base component should be known. At this stage control interval and control type (some of non-destructive test methods) should be defined.

d) Documentation: correct and complete documentation of all undertaken activities, as well as quality insurance, represent the evidence of good work and valuable source of future repair jobs.

References

[1] Domazet, Ž., Engineering Failure Analysis, Vol. 3, No. 2, (1996), pp. 137-147.

[2] Domazet, Ž., Lozina, Z., Piršic, T., Mišina, N., Đukic, P., FESB Report No. 01/99, Split (1999).

[3] Domazet, Ž., Barlè, J., Đukic, P., FESB Report No. 14/01, Split (2001).

Željko Domazet[1], *Francisko Lukša*[1], *Lovre Krstulović-Opara*[1]

Failure analysis of the rolls with grooves

[1]Faculty of Electrical Engineering, Mechanical Engineering and Naval Architecture; University of Split; Split, Croatia

Abstract

The failure analysis of the rolls with grooves on the 3-high-roughing mill stand for hot rolling is presented. Detailed analysis of all the elements which influenced the failure was carried out, namely: the position and the place of all failures are determined and all fracture surfaces are described; the rolling forces are determined by analytical and experimental methods; numerical analysis of the local stresses due to rolling forces is performed with finite element method; stress time history of the individual local stress and stress spectrum are obtained from service loads; properties of the roll material (strength, hardness, toughness and ductility) is determined by experimental testing. Based on the results of investigation, main causes of failures are presented.

***Keywords**: failure analysis, roll failures, hot rolling*

1. Introduction

In "Steelworks Split" failures of the rolls with grooves on the 1st stand of the 3-high-roughing mill stand (Fig.1) occurred four times. The 3-high-roughing mill stand was suitable for the hot rolling of the billets with an initial cross-section of 100 mm square and 3 m initial length in 8 passes. The mass of one billet was 230 kg.

Fig. 1. 3-high-roughing stand

The length of the roll was 2300 mm, roll barrel length was 1400 mm and roll barrel diameter was 450 mm. Roll speed was 120 rpm. The material used for the rolls was spheroidal graphite iron with the pearlitic base. Hardness on the roll surface was 380 HB. The rolling material was BSt 400 S according to DIN 488. Rolling temperature of the rolling material in the first pass was 1200°.

The pass schedule and corresponding dimensions are given in Table 1. Figure 2 shows the roll design and groove distributions with positions of the failures.

Table 1. Pass schedule

Pass No.		1	2	3	4	5	6	7	8
Pass shape		box	box	box	box	box	oval	square	oval
Groove dimensions [mm]		100x82	100x66	67x80	67x59	66x52	80x34	40	58x20
Cross-section [mm^2]	9850	8015	6474	5398	4032	3280	2286	1578	1075
Width [mm]	100	104	108	71	76	65	82,5	53,5	60,5
Initial height [mm]		100,0	82,0	108,0	80,0	76,0	52,0	82,5	40,0
Height after pass [mm]		82,0	66,0	80,0	59,0	52,0	34,0	51,0	20,5
Absolute draught [mm]		18,0	16,0	28,0	21,0	24,0	18,0	31,5	19,5
Absolute reduction [mm^2]		1835	1541	1076	1366	752	994	708	503
Coefficient of elongation		1,23	1,24	1,20	1,34	1,23	1,43	1,45	1,47
Working diameter [mm]		372,5	393,5	372,5	398,5	396,5	419,5	397,25	433
Length [m]	3	3,69	4,56	5,47	7,33	9,01	12,93	18,73	27,49
Projected length of contact arc [mm]		57,84	56,10	72,08	64,68	68,97	61,44	79,10	64,97
Projected area of contact [mm^2]		5900	5947	4938	4754	4276	4531	3461	3265
Rolling time [s]		1,58	1,74	2,26	2,65	3,53	4,65	6,92	9,52
Gap [s]		3	3	3	3	3	3	3	3
Rolling temperature [°C]	1200	1198	1194	1188	1183	1176	1169	1159	1146

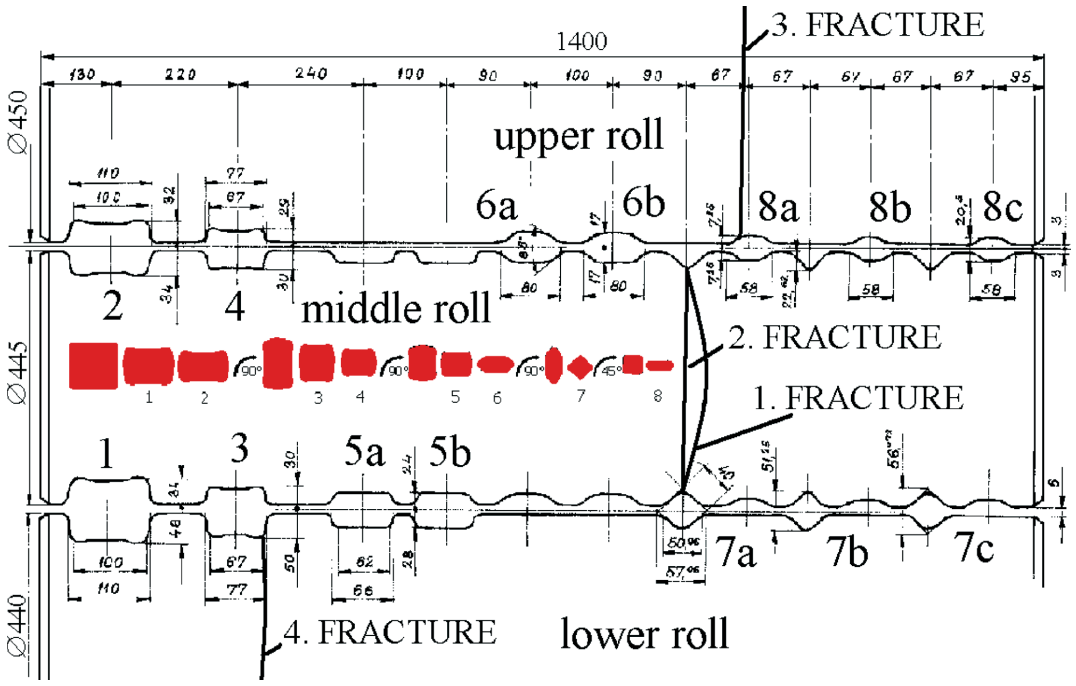

Fig. 2. Roll design and groove distributions

2. Fractures of the rolls

The first roll (middle roll) broke after 13 hours of operation. Figure 3 shows the position of the 1st fracture.

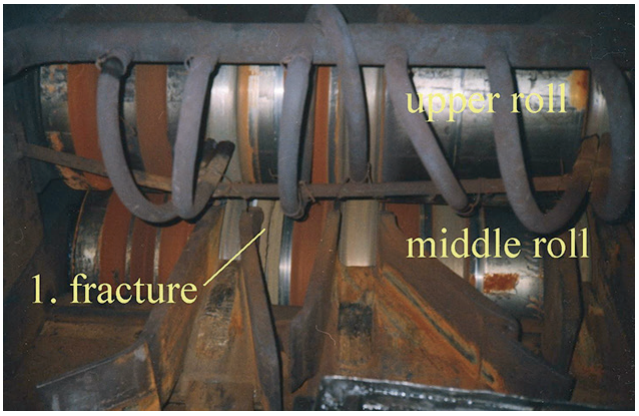

Fig. 3. Position of 1st fracture (back side of the stand)

Figure 4 shows the fracture surfaces of the 1st broken roll with the position of the stocks at the time of the fracture.

The second roll (middle roll) was dressed after 4000 rolling tons and broke after 10 hours of operation after

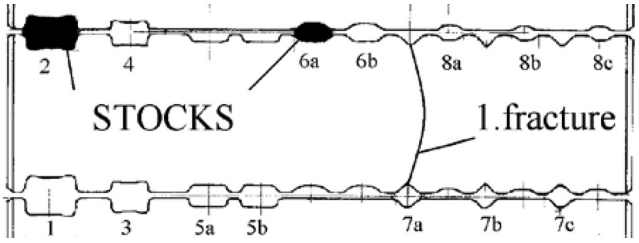

Fig. 4. Fracture surfaces of the 1st broken roll and the position of the stocks at the time of the fracture

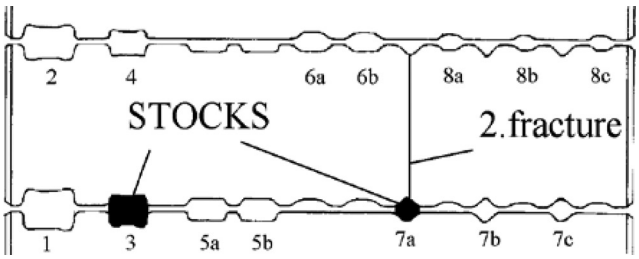

dressing. Figure 5 shows the fracture surfaces of the 2nd broken roll with the position of the stocks at the time of the fracture.

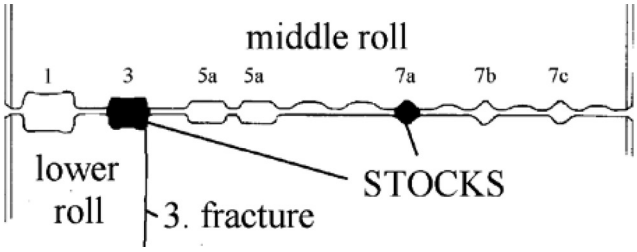

The third roll (lower roll) was dressed two times, after 4000 rolling tons and then after 8000 rolling tons. This roll broke after a short time of operation after the second dressing. Figure 6 shows the third broken roll and the fracture surface with the position of the stocks at the time of fracture.

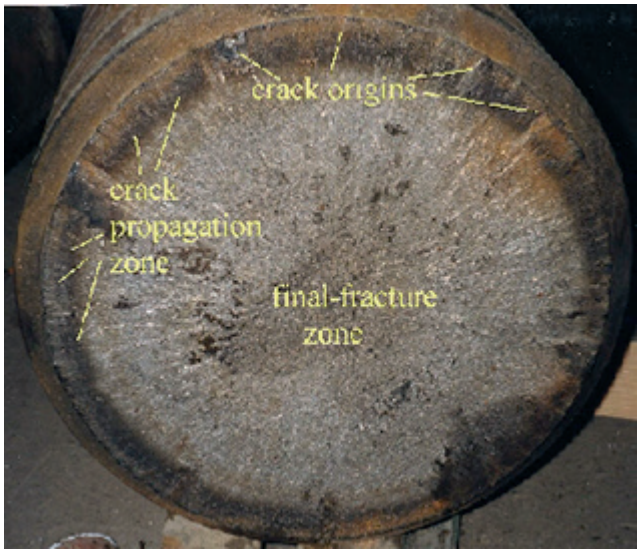

Fig. 5. Fracture surfaces of the 2nd broken roll and the position of the stocks at the time of the fracture

Fig. 6. Fracture surfaces of the 3rd broken roll and the position of the stocks at the time of the fracture

The fourth roll (upper roll) was dressed after 4500 rolling tons and broke after 568 rolling tons after dressing. Figure 7 shows the fourth broken roll and the fracture surface with the position of the stocks at the time of the fracture.

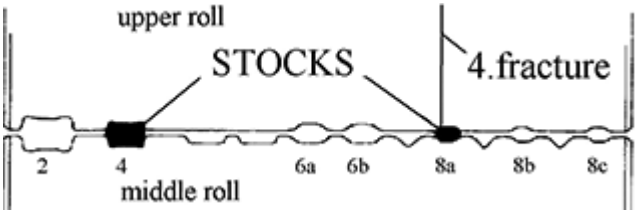

Fig. 7. Fracture surfaces of the 4th broken roll and the position of the stocks at time of the fracture

Visual examination of the fracture surfaces of the 1st , 2nd and 4th broken roll revealed three fracture regions as shown in Fig. 4, Fig. 5 and Fig. 7: crack origin zone on the periphery, crack propagation zone and final fracture zone. The fracture surfaces of the 2nd and 4th broken roll were flat while the fracture surface of the 1st broken roll was curved. No surface irregularities and no fire cracks were present in the fracture surfaces and around the fracture surfaces on the surface of the grooves. The appearance of the fracture surfaces suggested low-cycle fatigue resulting from rotational-bending loading with a high stress concentration.

Visual examination of the fracture surface of the 3rd broken roll revealed only one fracture region with rough striations from the surface to the centre of the roll. The appearance of the fracture surface of this roll suggested that the fracture occurred rapidly due to overload by dynamic impact.

3. Rolling forces

There are several methods used nowadays to calculate the rolling force (A.I.Tselikov, S.Ekelund, A.A.Korolev, A.Geleji, A.F.Golovin and V.A.Tiagunov, R.B.Sims and E.Siebel), and the results of them all are different. Because of numerous parameters (properties of the rolls and rolling material; form of the grooves; the friction between rolls and rolling material…) experimental methods are more suitable for determining the rolling force in the grooves.

In accordance with results from analytical methods for determining the rolling force, four measuring devices with three strain gauges on each, were designed for the experimental determination of rolling force (Fig. 8). The

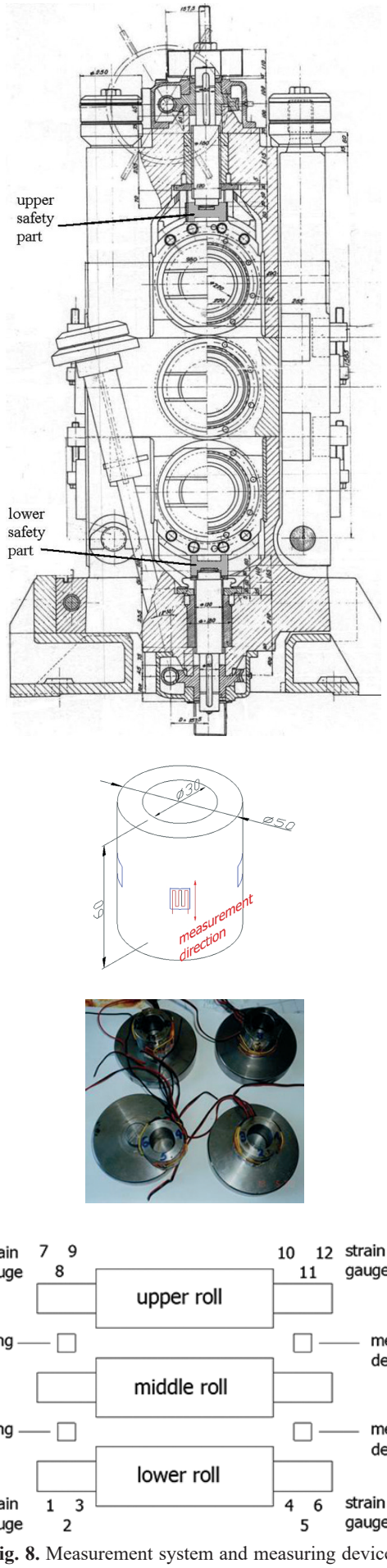

Fig. 8. Measurement system and measuring devices

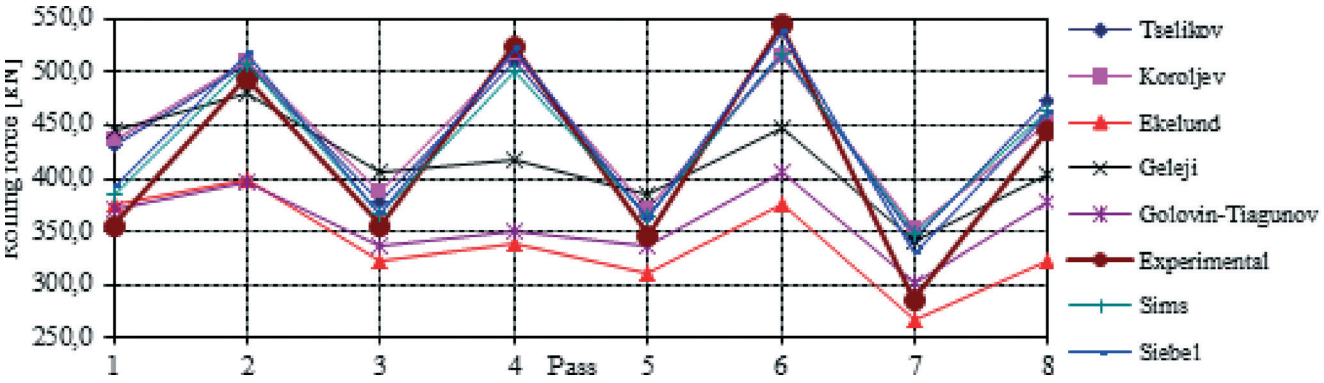

Fig. 9. Analytical and experimental results

measuring devices were mounted on both sides of the stand, instead of safety parts against the breakage of rolls (Fig. 8).

Figure 9 shows the experimental and analytical results.

4. Stress-time history

The obtained experimental results of the rolling forces are used for numerical analysis of the local stresses by finite element method. The FEM revealed that the most critical area of the roll is 7.a pass. The linear elastic model with 3D solid elements with eight DOF per nodes was used. The complete numerical analysis included 30 cases according to the rolling schedule. Fig. 10 shows the FEM model of the middle roll with the positions of the stocks in 4. and 8.a passes and maximum stress amplitudes of approximately 85 MPa in the 7.a pass.

Stress time history of the individual local stress and stress spectrum are obtained from numerical analysis and pass schedule. Figure 11 shows stress time history of the local stress in the 7.a pass for only one billet.

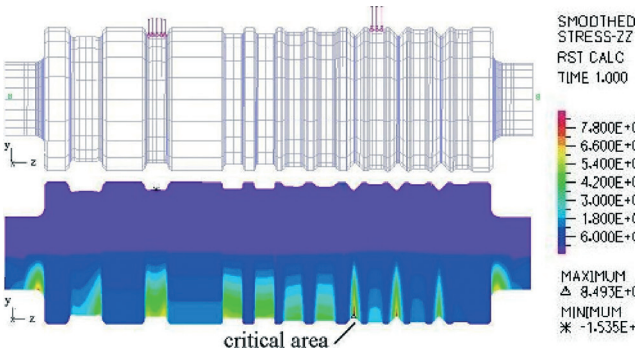

Fig. 10. Numerical analysis

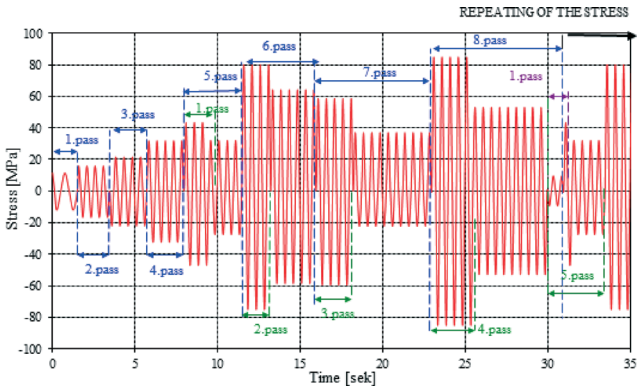

Fig. 11. Stress time history at the critical area for one billet

5. Material

The material used for rolls is spheroidal graphite iron with the pearlitic base. Chemical composition of the roll material is 3.4÷3.6 % C, 1.8÷2.2 % Si, 0.5÷1 % Mn, < 0.05% P, < 0.05% S, < 0.5% Cr, 1.5÷3% Ni and <0.2% Mo. Hardness on the roll surface is 380 HB. Fig. 12 shows hardness drop of KGR 380 rolls and metallographic structure of the roll material.

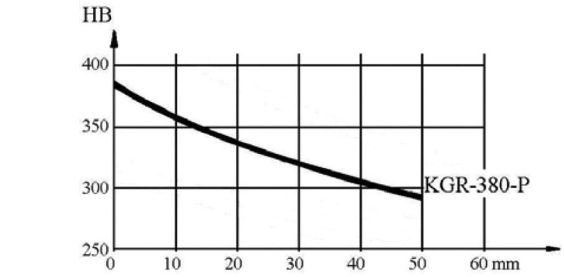

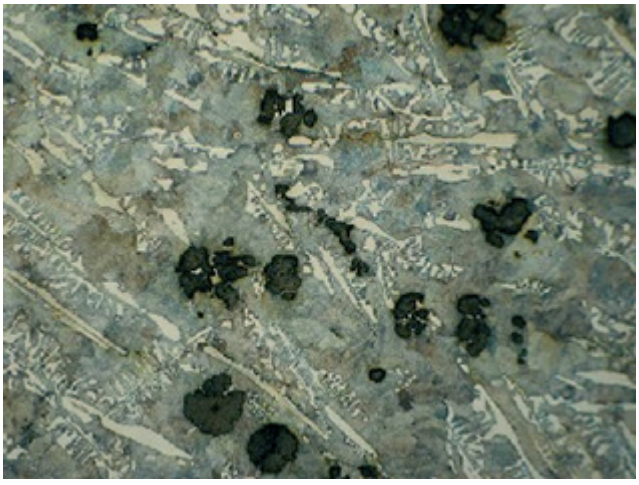

Fig. 12. Hardness drop and metallographic structure (500x)

Tensile strength of the core is 325÷425 MPa and bending strength of the core is 500÷700 MPa. Because of the technical data of the material for fatigue duration prediction from working area of the rolls was omitted, fatigue strength was determined by experimental testing.

Figure 12 shows fatigue strength of the roll material and stress spectrum in the critical area for 4000 rolling tons.

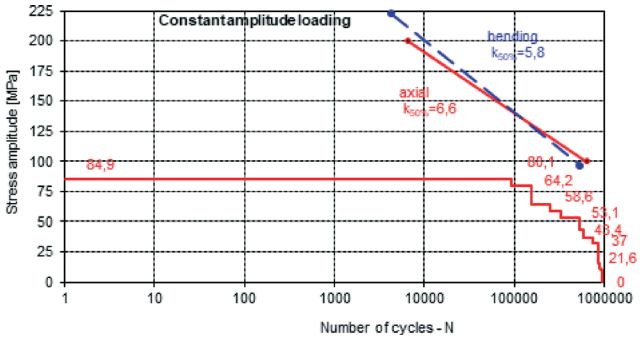

Fig. 13. Fatigue strength of the roll material and stress spectrum in the critical area for 4000 rolling tons

This diagram reveals that failures should be avoided in normal service without overloads.

6. Overloads and safety parts

The temperature of the rolling material has a great influence on the rolling forces. When the rolling process is carried out at a decreased temperature, the rolling forces are higher and bending stresses can be two or three times higher than usually (Fig. 14).

During the rolling process some of the rolling stocks stayed on the rollers outside of the furnace due to technological stops. The temperatures of these stocks decreased due to cooling by ambient air. No sensors of the temperature of a rolling stock between the furnace and 3-high-roughing mill stand were anticipated and there was no control of decreasing rolling temperature between the furnace and 3-high-roughing mill stand. Because of this fact the rolls were occasionally subjected to higher rolling forces and bending overloads as the result of technological stops.

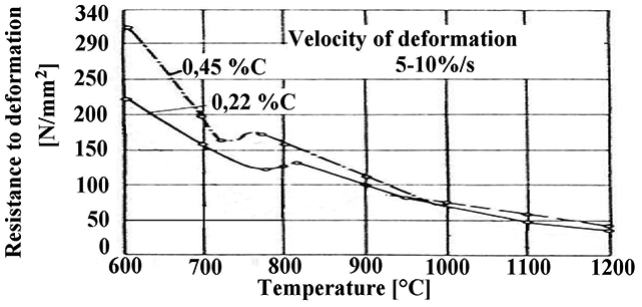

Fig. 14. Resistance to deformation of carbon steels related to temperature

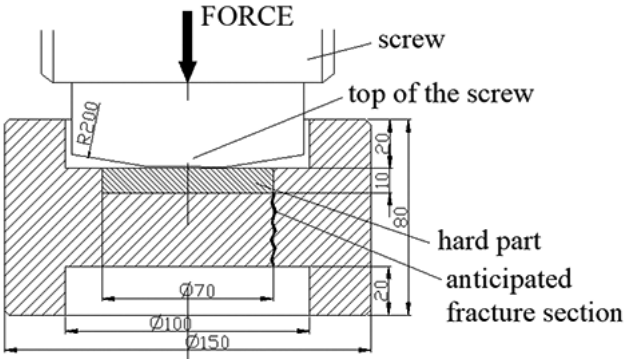

Fig. 15. Safety part

The rolls are protected from bending overload with the safety parts (Fig. 8). In case of the bending overload, one (or both) safety part has to fail before the failure of the roll. The material used for safety parts was flake graphite iron GG20 according to DIN. Figure 15 shows the safety parts design.

Analysis of safety parts design showed that the safety parts have to fail if the rolling temperature is 900°C.

In all cases of the roll failures, the failure of safety parts did not occur.

8. Concluding remarks

The following general conclusions were drawn out from the described analysis:

Three out of four rolls fractured due to the low-cycle fatigue resulting from the rotational-bending loading with high stress concentration. The fracture of the fourth roll occurred rapidly due to the bending overload by dynamic impact.

The bending overload was the result of the decreasing rolling temperature due to technological stops.

Safety parts, designed to prevent failure of the rolls, did not perform their function.

According to the above conclusions the next corrective measures were proposed:

- Change of the roll designs and groove distributions according to the pass schedule.
- To install the devices for the control of the rolling temperature during the whole rolling process.
- Change of the safety parts design.

The first and the second measures were performed during the modernization and reconstruction of the plant.

References

[1] F. Lukša. Investigation of the cause of the failures of the rolls with grooves. Master Thesis, University of Split, Faculty of Electrical Engineering, Mechanical Engineering and Naval Architecture, Split, Croatia: 2005.

[2] Ž. Domazet, F. Lukša. Experimental determination of the rolling force on the rolls with grooves. Proceedings of the 22-nd Symposium "DANUBIA-ADRIA" on Experimental Methods in Solid Mechanics, Parma, Italy: 2005.

Željko Domazet[1], *Francisko Lukša*[1], *Miro Bugarin*[1]

Failure of two overhead crane shafts

[1]Faculty of Electrical Engineering, Mechanical Engineering and Naval Architecture; University of Split; Split, Croatia

Abstract

The failure analysis of two overhead crane shafts is presented: the failure of an overhead crane drive shaft and the failure of an overhead crane gearbox shaft, due to rotating-bending fatigue. The fracture of the overhead crane drive shaft originated in small radius fillet between two different diameters of the shaft. A new shaft was made with a larger-size fillet, resulting in reduced stress concentration in this region. The failure of the overhead crane gearbox shaft originated in the intersection of two stress raisers, due to a change in the shaft diameter and in the keyway corner. A new shaft was made with a larger-size fillet and a larger size radius of the keyway corner to minimize stress concentration in this section. In both cases the installed couplings were replaced by gear couplings in order to allow parallel and angular misalignment as well as to avoid additional load due to misalignment. The analysis shows that the fatigue life can be significantly increased with a simple change in the structural details

Keywords: *Failure analysis; Shaft failures; Overhead cranes*

1. Introduction

The fatigue fractures of shafts originate at points of stress concentration, such as changes in the shaft diameter and ends of the keyways. The sharp corner at the intersection between two different diameters of the shafts or in the bottom of the keyway can cause local stress to be few times greater than the average nominal stress. The failure analysis of an overhead crane trolley drive shaft is presented in the first part of this paper. The failure originated in the radius fillet between two different diameters of the shaft. The failure analysis of an overhead crane trolley gearbox shaft is presented in the second part of the paper. The failure of this shaft originated at the intersection of two stress raisers, the change in the shaft diameter and keyway.

2. Failure of overhead crane drive shaft

In "Steelworks Split" the high-speed electric overhead crane, Fig.1, was suitable for transport of the billets from the melt shop to the rolling mill hall. The crane was rated at 10 tons with a span of 20.5 m and handled about 100 lifts and transports per day, each lift averaging 5 tons. The stepped drive shaft used for an overhead crane trolley wheel fractured after 24 months of service. The electric motor power rating was 3 kW with an output speed of 940 rpm. The maximum travel speed of the trolley was 32 m/min.

The shaft was connected with the gearbox by a roller chain coupling, supported by two roller bearings and connected with the wheel by a key, Figure 2.

The shaft was made of quenched and tempered steel 25CrMo4 according to German standard DIN (Deutsches

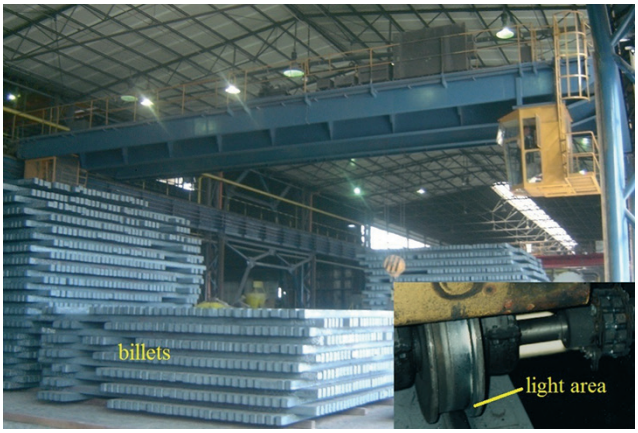

Fig. 1. Overhead crane for transport of billets

Institut für Normung) [1]. The chemical composition of material was verified by using quantometer. The hardness and the microstructure were confirmed to be tempered steel 25CrMo4. The fracture occurred on the fillet

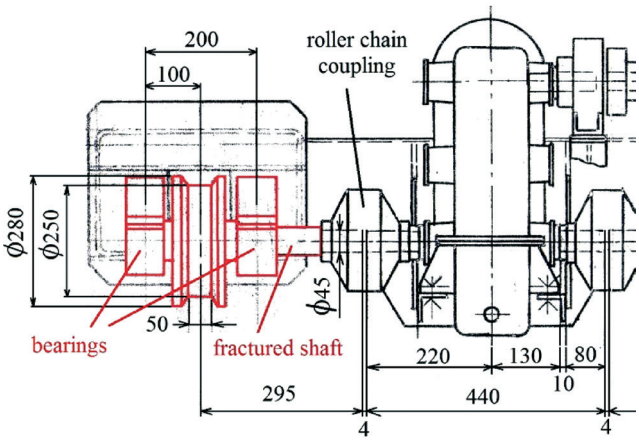

Fig. 2. Overhead crane trolley [2]

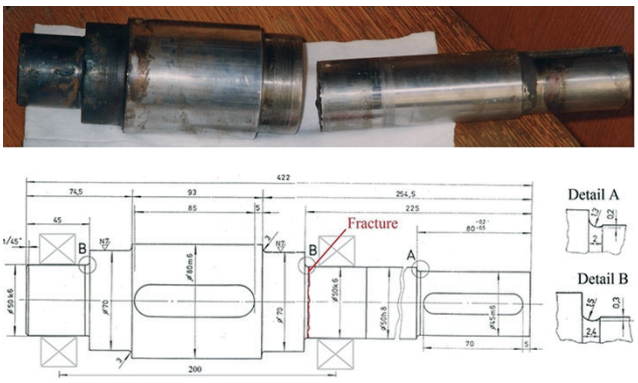

Fig. 3. Stepped drive shaft

due to change between two different diameters of the shaft approximately 225 mm from the driven end and approximately 30 mm from one end of the keyway where the crane wheel was keyed to the axle, Figure 3.

2.1. Fracture surface investigation

The contour of the fracture surface was convex with respect to the smaller-section side. There were three fracture regions, Figure 4: a region of multiple crack origins around the outer perimeter (at A); a region of the crack propagation zone (at B); and a region of the final, fast fracture (at C).

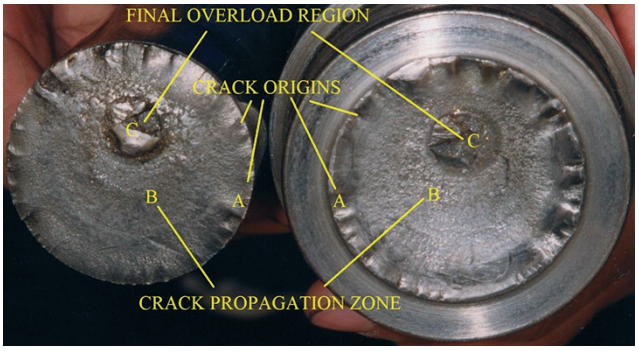

Fig. 4. Fracture surfaces

The presence of multiple crack origins separated by ratchet marks around the outer perimeter was an indication of rotational-bending fatigue with severe stress concentration.

The relatively small size of the final fracture region was an indication of low nominal stress. In rotational-bending, during each revolution, every point of the shaft circumference was subjected to tensile-compressive stress and therefore the crack could be initiated at any point on the shaft periphery.

The individual cracks propagated toward a single crack front, region B, Figure 4. The crack surfaces were pressed together during the compressive component of the stress cycle, and mutual rubbing occurred. The beach marks were not visible because they were obliterated by rubbing.

The conclusion from the surface investigation was that the shaft fractured as a result of rotational-bending fatigue. The primary cause of the fracture was the bending load during the rotation, although the total load was a combination of bending and torsional loads. The small radius of the fillet at a change in shaft diameter, detail B in Figure 3, resulted in high stress concentration, which initiated the crack.

The visual examination of the wheel and rail revealed smooth and light contact area on the sides of both parts due to mutual rubbing, detail in Figure 1, which was caused by additional torsional load. Post-failure verification of parallelism and straightness of the rails with optical instrument revealed misalignment in parallelism and straightness.

2.2. Stress analysis

2.2.1. Bending stresses

During normal operation, bending stresses in the critical area were caused by a wheel vertical load. The wheel vertical load was considered as a force applied at the center line of the wheel contact with the shaft, see Figure 5. The applied force was calculated from the design load, see reference [2].

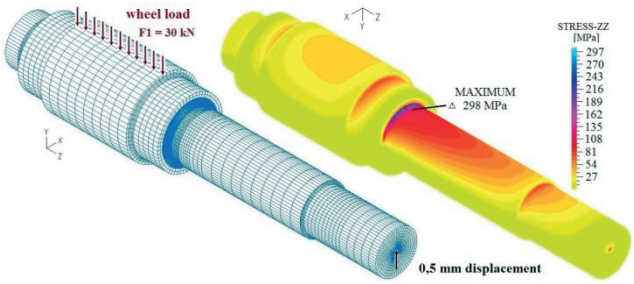

Fig. 5. Numerical analysis

A numerical analysis of local stresses was done by the finite element method using ADINA software. The linear elastic model with 3D solid elements with eight DOF per nodes was used, Figure 5. Each node had 3 degrees of freedom, translation in X, Y and Z direction. The model is fixed in the line on the positions of bearing centers and loaded with concentrated forces in the nodes. The numerical analysis of local stresses revealed that design force due to vertical load should not have led to shaft fracture. Force 30 kN caused local stresses of 79 MPa in the critical area.

Post-failure verification revealed parallel misalignment of 0.5 mm between two shaft axes. The numerical analysis of local stresses revealed that displacement of 0.5 mm caused an increase in local stresses in the critical area three times (298 MPa), Figure 5.

A roller chain coupling was used to transmit power between shafts. The torque was transmitted through a double roller chain. Due to clearances between the chain and the sprocket teeth on two couplings, the roller chain coupling permitted eccentricity – ε (parallel misalignment) between shafts up to 2% of the roller chain pitch

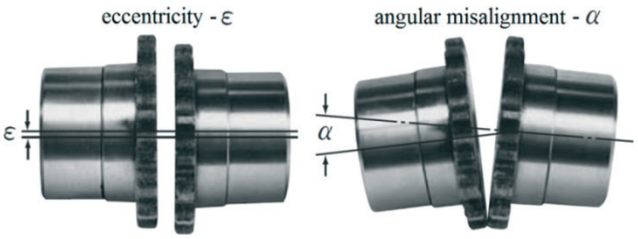

Fig. 6. Roller chain coupling [3]

and angular misalignment – α between shafts up to 1°, [3], see Figure 6.

If eccentricity and angular misalignment between the wheel shaft axis and the drive axis is higher than the chain coupling can compensate, there is a vertical force on the end of the wheel shaft and also corresponding additional bending stresses in the critical place.

2.2.2. Torsional stresses

The maximum applied torque of 716 Nm in the drive shaft was estimated from the electric motor power rating of 3 kW, the maximum travel speed of the trolley of 32 m/min and the wheel diameter was 250 mm. The calculated nominal shear stress for the shaft diameter of 50 mm was 28.6 MPa. The stress concentration factor due to torsional stress at a change of the shaft diameter according to literature [4] was 1.8. The maximum shear local stress at the intersection of the change of the shaft diameter due to stress concentration was 51.5 MPa.

From the comparison between bending and shear stresses it was concluded that bending stresses were dominant for the shaft fracture.

2.3. Corrective action

A corrective action was considered in two ways:

a) Decreasing the stress concentration in the critical area by increasing the size of the fillet radius and

b) Reducing the influence of parallel misalignment between the shaft axis and coupling axis on local stresses by changing the type of the coupling, which permitted more parallel misalignment between axes.

2.3.1. Increasing the size of the fillet radius

The distance between the large diameter of the shaft (wheel) and the bearing was 11 mm, Figure 7. The spacer was positioned between the wheel and bearing. Increasing the size of the fillet radius was limited by the design of the spacer.

Therefore, numerical experiments were carried out for four different sizes of the fillet radius in order to reduce local stresses below the endurance limit, Figures 8 and 10.

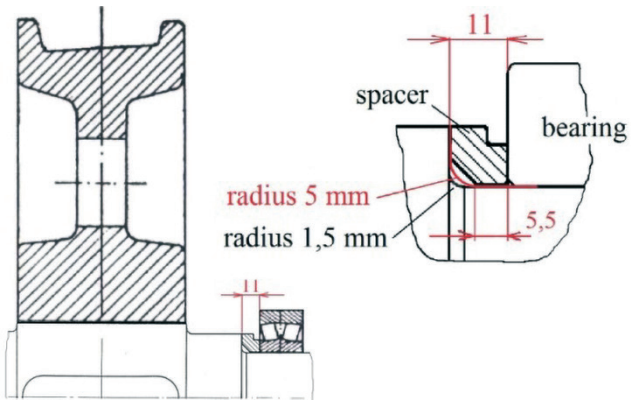

Fig. 7. Design of the spacer

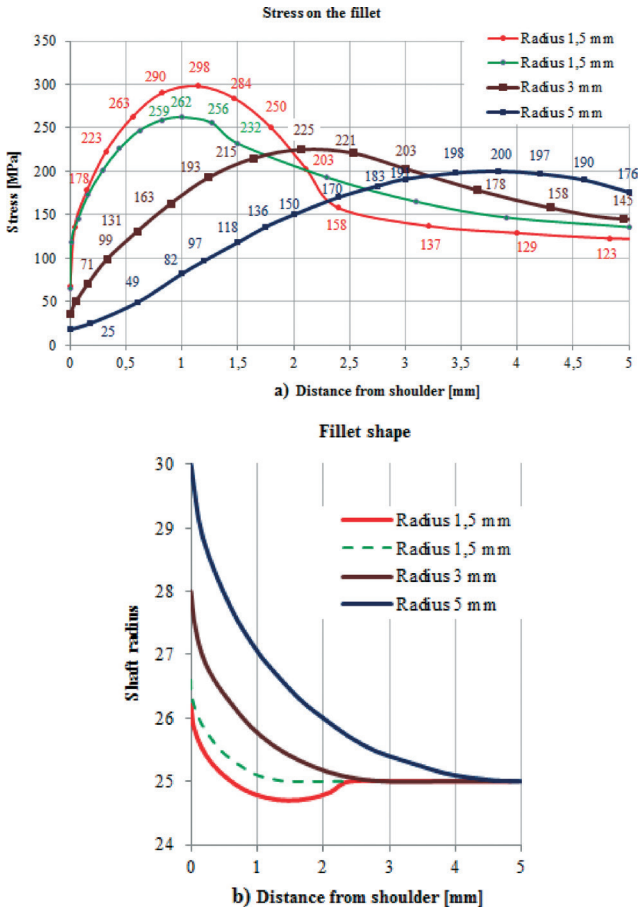

Fig. 8. Stress distribution

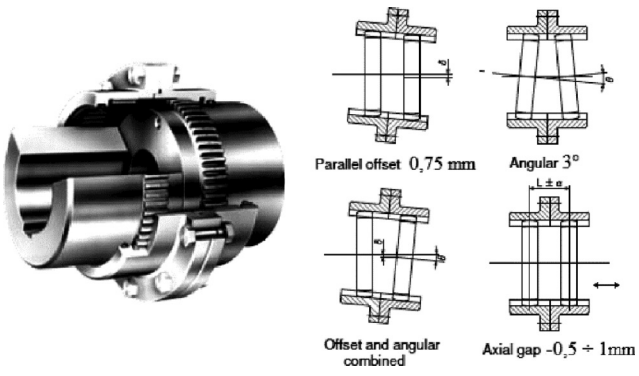

Fig. 9. Gear coupling, [7]

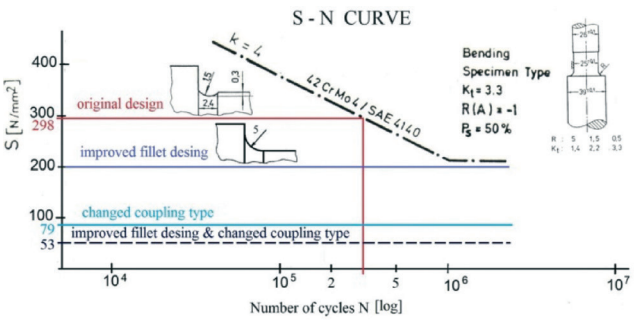

Fig. 10. Influence of corrective actions on fatigue life

The stress concentration factors in the critical areas had a good agreement with literature [4] and [5]. The fatigue strength curve of the material was used from literature [6].

The curves in Figure 8 show the increasing size of the fillet radius from 1.5 mm to 5 mm, reducing maximum local stress by about 1.5 times (from 298 to 200 MPa).

2.3.2. Change of the coupling type

A gear coupling was considered to substitute the roller chain coupling, Figure 9. The gear coupling can accommodate more eccentricity and angular misalignment than the roller chain coupling. According to [7], the gear coupling permits parallel offset 0.75 mm, angular 3° and axial gap from -0.5 to 1 mm. Since post-failure verification revealed parallel misalignment of 0.5 mm between two shaft axes, the application of the gear coupling in this case can eliminate force on the shaft due to misalignment and can also reduce local stresses in the critical area.

Figure 10 shows the influence of considered corrective actions on fatigue life.

The actual service life was estimated from the working time of the crane, the number of liftings and the wheel diameter. The crane was in service for about 400 working days in the period of two years. The average number of transports per day was 100 with the travel of the trolley 10 m per each transport. For the wheel diameter of 250 mm and the corresponding shaft the actual service life was about $4.8 \cdot 10^5$ cycles. The estimated service life from the numerical model was about $3 \cdot 10^5$ cycles, Figure 10.

The redesign of the shaft fillet radius from 1.5 mm to 5 mm reduced maximum local stress below the fatigue endurance limit (about 90% of endurance limit). The application of a gear coupling to accommodate parallel misalignment reduced maximum local stress to about 35% of the endurance limit, what was more than two times in comparison to the redesign of the shaft fillet radius. A combination of the fillet radius redesign and the application of the gear coupling additionally reduced local stresses, Figure 10.

Based on this analysis, the actual service life of the shaft can be improved from the finite (about $4.8 \cdot 10^5$ cycles) to the infinite lifetime.

2.3.3. Correction

New shafts were made from quenched and tempered steel 42CrMo4 according to DIN [1] with a larger-size fillet, which minimized stress concentration in this region and prevented recurrence of the failure. The roller chain couplings were replaced by gear couplings to reduce the influence of parallel misalignment between the shaft axis and coupling axis on local stresses.

3. Failure of overhead crane gearbox shaft

An electric overhead crane, Fig. 11, was suitable for the transport of a ladle with liquid steel from the ladle furnace to the continuous casting machine. The crane was rated at 50 tons with a span of 18.4 m and handled about 20 lifts and transports per day, each lift averaging 43 tons. The stepped drive shaft used in an overhead crane trolley gearbox, Figure 12, broke after 36 months of service.

The electric motor power rating was 5.5 kW with an output speed of 940 rpm. The maximum travel speed of the trolley was 20 m/min. The overhead crane trolley gearbox [8] is shown in Figure 12 and the shaft is shown in Figures 13 and 14.

Fig. 11. Overhead crane for transport of ladle with liquid steel

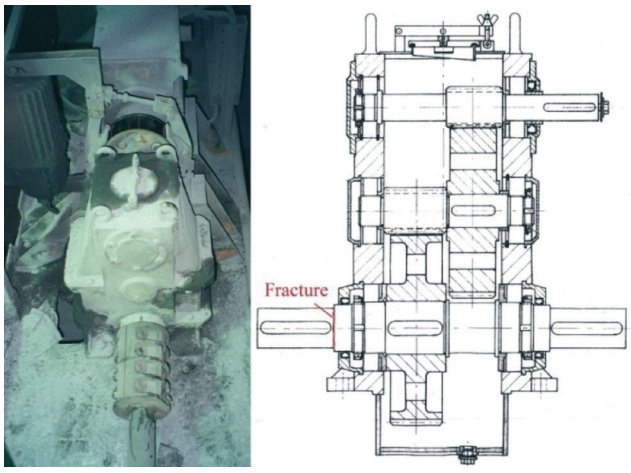

Fig. 12. Overhead crane trolley gearbox

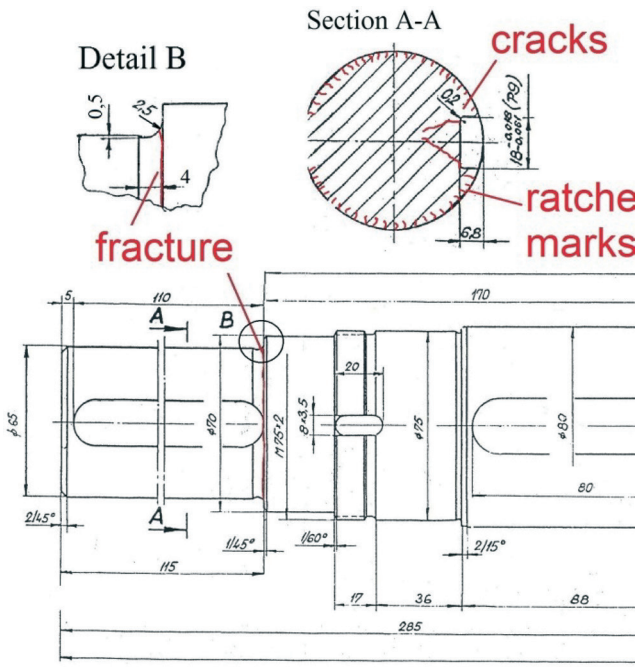

Fig. 13. Stepped drive shaft [8]

Fig. 14. Stepped drive broken shaft

3.1. Fracture surface investigation

The shaft was made of construction steel St 52-3 according to DIN [9]. The fracture occurred on a fillet due to change between two different diameters of the shaft approximately 110 mm from one end. The contour of the fracture surface was convex with respect to the smaller-section side.

There were four fracture regions, Figure 15. Numerous ratchet marks (at A), on the outer edge of the surface and the dark band at this edge indicate fatigue cracks initiation, what is a characteristic of rotational-bending fatigue. Two cracks (at B) from the keyway corners suggested torsional stresses. The cracks propagated circumferentially around the shaft (at C). The final fracture was a mixed ductile and brittle fracture in the middle of the elliptical contour (at D). The beach marks were not visible because they were obliterated by rubbing.

In this case there were two stress raisers in the same area: a sharp corner in the keyway and a change in the shaft diameter. Additionally, the end of the keyway was due to change in the shaft diameter, fracture section in Figure 13, causing high concentration of stresses.

The conclusion from the surface investigation was that the shaft fractured as a result of the rotational-bending fatigue due to high stress concentration. The cracks were initiated

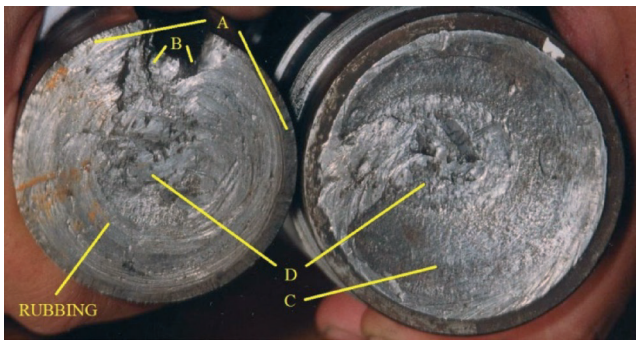

Fig. 15. Fracture surfaces

in the intersection of two stress raisers, on the sharp corner in the keyway and on the radius of the fillet due to change in the shaft diameter, detail B in Figure 13.

3.2. Stress analysis

3.2.1. Bending stresses

A split muff coupling was used to transmit power between the shafts, Fig.12.

The split muff coupling is a type of rigid coupling and should be used when the alignment of the two shafts can be maintained very accurately. A small missalignment between two shafts can cause high stresses. Post-failure verification revealed parallel misalignment of 0.8 mm between the gearbox shaft axis and the drive shaft axis of the wheel, Figure 16.

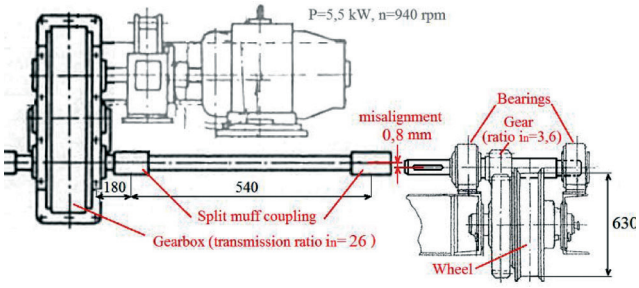

Fig. 16. Misalignment between the gearbox shaft axis and drive shaft axis of the wheel

The numerical analysis of local stresses was done by the finite element method using ADINA software. The applied force of F=15000 N was estimated from the parallel misalignment of d=0.8 mm according to expression (1), Figure 17, where l = 720 mm and a = 180 mm, Figure 16.

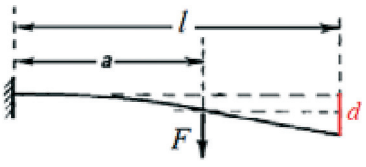

Fig. 17. Deflection

$$d = \frac{Fa^2}{6EI}(3l - a) \quad (1)$$

The linear elastic model with 3D solid elements with eight DOF per nodes was used, Figure 18. Each node had 3 degrees of freedom, translation in X, Y and Z direction. The model is fixed in the back side face and loaded with concentrated forces in the node on the front side.

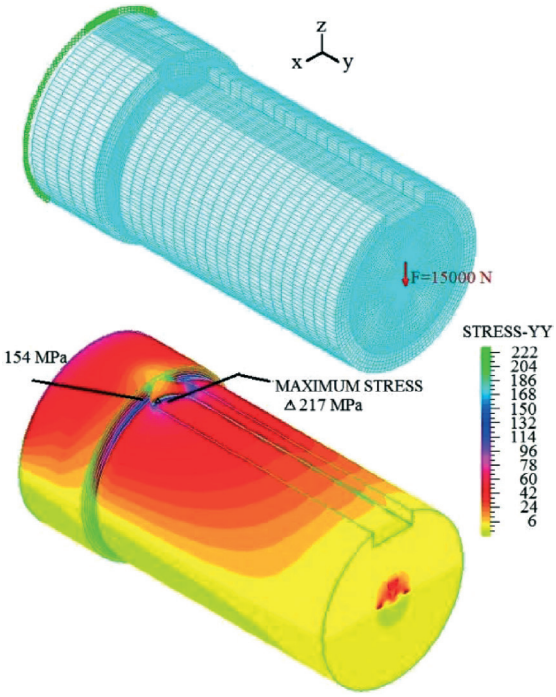

Fig. 18. Numerical analysis

The FEM analysis of local stresses revealed that the maximum stress 217 MPa was in the sharp corner of the keyway and the stress on the fillet due to change in the shaft diameter near the keyway was 154 MPa, Figure 18. Stress concentration factors in critical areas had a good agreement with literature [4] and [5].

3.2.2. Torsional stresses

The maximum applied torque of 1458 Nm in the gearbox output shaft was estimated from the electric motor power rating of 5.5 kW with an output speed of 940 rpm and the gearbox transmission ratio 26. The calculated shear stress for the shaft diameter of 65 mm was 26.5 MPa. The stress concentration factor due to torsional stress due to change of the shaft diameter was 1.5 and due to the keyway it was 1.7 [4]. The maximum local stress due to change in the shaft diameter and the keyway due to stress concentration was 67.6 MPa.

3.3. Corrective action

Corrective action were considered in both critical areas:

a) Increasing the fillet radius due to change in the shaft diameter from 2.5 mm to 4 mm, Fig. 19.

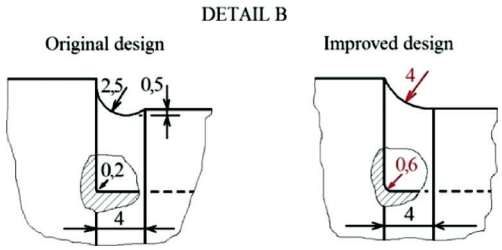

Fig. 19. Original and improved design of the fillet radius

b) Increasing the radius in the keyway corner of the maximum size. The maximum radius size in the keyway corner for the shaft diameter 65 mm according to DIN [10] was 0.6 mm, Fig. 19.

c) Reducing the influence of parallel misalignment between the shaft axis and coupling axis on local stresses by changing the type of coupling which permits parallel misalignment between axes.

3.3.1. Increasing both the radius in the keyway corner and the radius due to change in the shaft diameter.

The FEM analysis of local stresses after the redesign revealed decreasing the maximum bending stress in the sharp corner of the keyway from 217 MPa to 145 MPa as well as decreasing stresses of the fillet radius due to change in the shaft diameter from 154 MPa to 86 MPa, Figure 20.

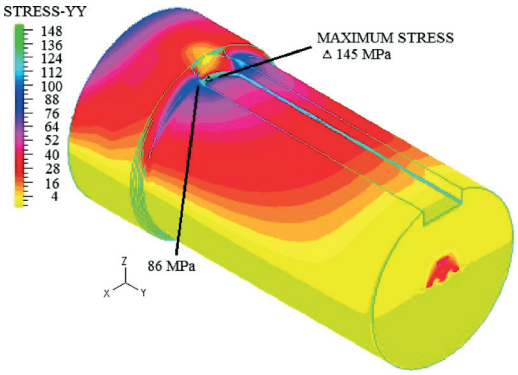

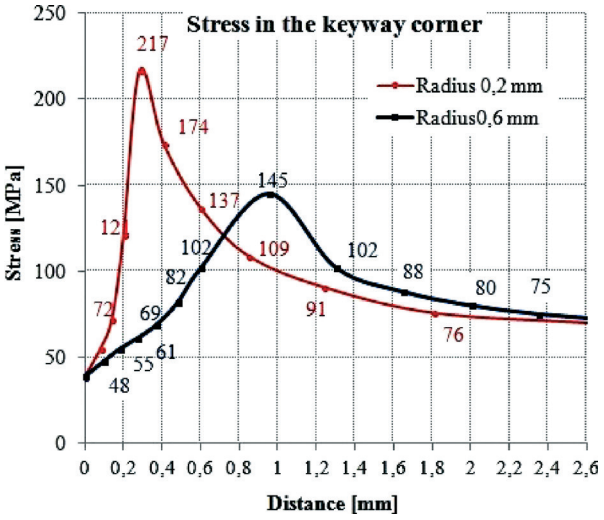

Fig. 20. Numerical analysis

3.3.2. Change of the coupling type

A gear coupling was considered to substitute the split muff coupling since post-failure verification revealed parallel misalignment of 0,8 mm between two shaft axes. The application of gear couplings can eliminate force on the shaft due to misalignment and can also reduce local stresses on the critical area.

Figure 21 shows the influence of considered corrective actions on the fatigue life. The fatigue strength curve of the material is used from literature [11].

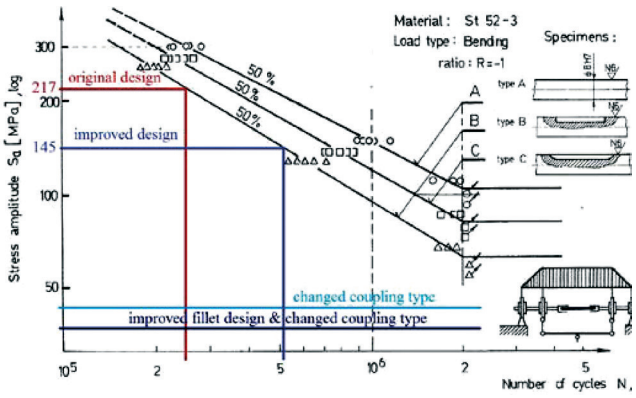

Fig. 21. Influence of corrective actions on the fatigue life

The actual service life was estimated from the working time of the crane, the number of liftings and the wheel diameter. The crane was in service for about 800 working days during a three year period. The average number of transports per day was 20 with the travel of the trolley 12 m per each transport. For the wheel diameter of 630 mm and the corresponding shaft, the actual service life was $3.5 \cdot 10^5$ cycles. The estimated service life from the numerical model was about $3 \cdot 10^5$ cycles, Figure 10.

The redesign of the shaft fillet radius reduced the maximum local stress and the estimated fatigue life was about two times longer according to actual fatigue life, Figure 21. The application of a gear coupling to accommodate parallel misalignment eliminated force due to misalignment, and bending stresses became negligible. A combination of the fillet radius redesign and application of the gear coupling additionally improved fatigue life.

Based on this analysis, the actual service life of a shaft can be improved from finite ($3.5 \cdot 10^5$ cycles) to infinite lifetime.

3.3.3. Correction

New shafts were made with the radius size due to change in the shaft diameter 4 mm and the radius size in the keyway corner 0.6 mm, minimizing stress concentration in both critical areas and preventing recurrence of the failure.

Split muff couplings were replaced by gear couplings to reduce the influence of parallel misalignment between the shaft axis and the coupling axis on local stresses.

4. Conclusion

The failure analysis of two overhead crane shafts showed that the overhead crane drive shaft and the gearbox shaft fractured as a result of rotational-bending fatigue. In both cases the fracture occurred on the places with high stress concentration. The fracture of the overhead crane drive shaft originated in the small radius fillet between two different diameters of the shaft. The fracture of the overhead crane gearbox shaft was initiated in the intersection of two stress raisers on the sharp corner in the keyway and on the radius of the fillet due to change in the shaft diameter. The failure analysis revealed that the design load should not have led to shaft fracture and that there also existed additional load unforeseen by the design. The post-failure verification in both cases revealed parallel misalignment between two shaft axes. Corrective actions were considered in two ways: to improve service life by a small change in the design and to remove the unforeseen additional load due to misalignment between two shaft axes.

In the case of the overhead crane drive shaft, increasing the size of the fillet radius from 1.5 mm to 5 mm decreased the maximum local stress below the endurance limit, resulting in significant increasing of the fatigue life. In the case of the overhead crane gearbox shaft, increasing the radius size due to change in the shaft diameter from 2.5 mm to 4 mm and the increasing of the radius size in the keyway corner from 0.2 to 0.6 mm extends the fatigue life more than twice. The gear coupling, compared to the roller chain coupling and especially to split muff coupling, allows more angular and parallel misalignment, prolonging significantly shaft service life. Based on this analysis, the actual service life of the shaft can be improved from finite to infinite lifetime.

References

[1] Deutsches Institut für Normung. DIN 17200, 1987 (DIN, Berlin)

[2] Crane design and manual book of billet overhead crane in "Steelworks Split"

[3] D.I.D., "Power transmission & conveyor chain", catalog, Daido Kogyo co, Kumasaka-Cho, Kaga-City, Ishikawa Pref, 922-8686, Japan, 2007.

[4] W.D. Pilkey, D.F. Pilkey, "Stress concentration factors", 3rd ed., Hoboken, John Wiley & Sons, New York, 2008.

[5] E. Heibach, "Betriebfestigkeit", VDI Verlag Gmbh, Düsseldorf, 1989.

[6] V. Grubišić, G. Jacoby, "Fracture analysis, validation and technologies to increase the strength of materials", Seminar, Firenze, March 1995.

[7] SEISA, "Gear coupling", catalog, Seisa Gear Ltd., Kaizuka, Osaka, Japan, 2011.

[8] Crane design and manual book of ladle overhead crane in "Steelworks Split"

[9] Deutsches Institut für Normung. DIN 17100, 1980 (DIN, Berlin)

[10] Deutsches Institut für Normung. DIN 6885-1, Paßfedern nuten, 1968 (DIN, Berlin)

[11] Ž. Domazet, "Fatigue stress concentration factor for shaft with different keyways in bending ", Osterreichische Ingenieur und Architekten Zeitschrift, 142. Jg., Heft 6/1997

Željko Domazet[1], Francisko Lukša[1], Petra Bagavac[1]

Failure analysis of the rolling mill stand coupling

[1]Faculty of Electrical Engineering, Mechanical Engineering and Naval Architecture; University of Split; Split, Croatia
[2]Steelworks Split d.d., 21212 Kaštel Sućurac, Croatia
[3]Bit-art informatika, Split, Croatia

Abstract

The failure analysis of two slipper couplings showed that both couplings fractured as a result of fatigue. In both cases, the fracture started in the corner between the paddle and the coupling body and propagated around the corner. Both fractures were caused by the deficient design of the fillet between the paddle and the coupling body with high stress concentration. In order to extend actual service life, three design modifications were considered. Numerical analysis showed that the redesign of the coupling with stiffener between the paddle and the coupling body reduced maximum local and actual service life of couplings and can be improved from finite to infinite.

***Keywords**: failure analysis; slipper coupling, fatigue*

1. Introduction

The roughing mill is one of the most loaded parts of the steel plant; it consists of two reversing 3-high mill stands with ten passes, eight on the first stand and two on the second, Fig.1. The failures of the rolls with grooves on the 1st stand of the 3-high-roughing mill stand occurred four times, Ref. [1]. The failures of the slipper coupling between the gearbox and the roughing mill occurred 2 times, Fig.2. The first coupling had been in service for 3.5 years when the coupling failure occurred. A failure of the second coupling occurred when the coupling had been in service for almost 4 years.

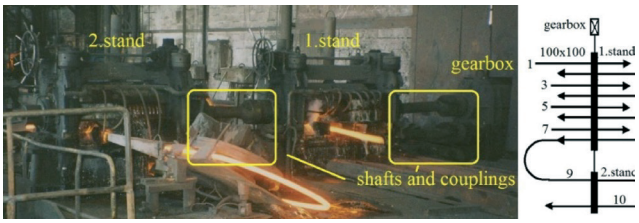

Fig. 1. Roughing mill [1]

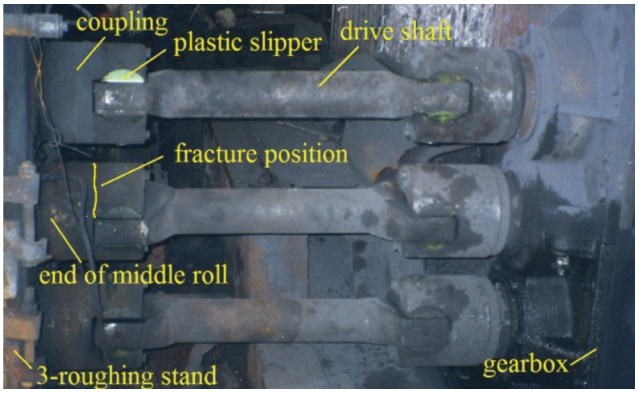

Fig. 2. Shafts and couplings between the 3-high-roughing stand and the gearbox

Slipper couplings and drive shafts are used to transmit torque between gearbox and 3-high-roughing mill stands. A failure of both couplings occurred on the middle roll between the first stand and the gearbox, roll side, Fig.2.

2. Failure of couplings

The couplings were made of quenched and tempered steel 30CrNIMo8 according to German standard DIN (Deutsches Institut für Normung), Ref.[2]. The chemical composition of the material was verified by using the quantometer. The hardness readings and microstructure indicated that the coupling had been satisfactorily heat treated by quenching and tempering. The fracture occurred two times in the groove between the paddle and the coupling body, Fig.3.

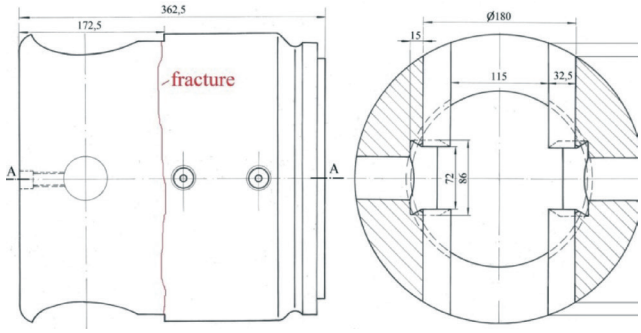

Fig. 3. Coupling drawing and fracture position

2.1. Fracture surface investigation

The first broken coupling is shown in Fig.5 and Fig.6. On the fracture surface of the first coupling there are four fracture regions, Fig.6: two regions of two fracture origins (at 1 and 2), the region of progressive fatigue crack propagation with curved beach marks (at 3), and the final fast fracture zone (at 4).

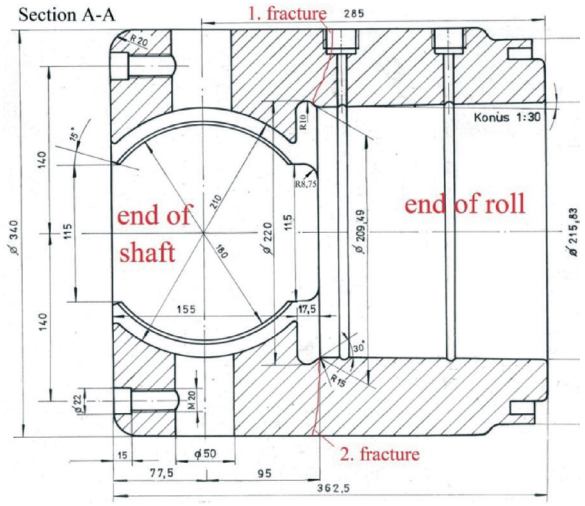

Fig. 4. Coupling drawing – Section A and fracture position

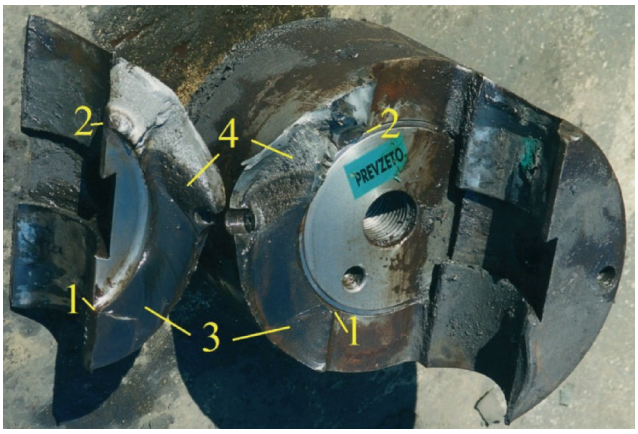

Fig. 5. Fracture of 1st coupling

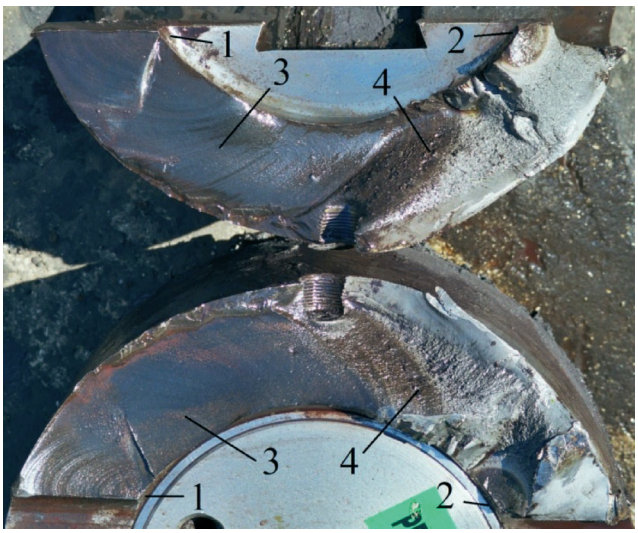

Fig. 6. Fracture surface of 1st coupling

The crack started in the corner of region 1 and propagated around this corner, what can be visible with curved beach marks.The final fracture occured when the region of progressive fatigue crack propagation reached about 60% of the paddle cross section, practically connected with another weak point – oil chanel.

The second broken coupling is shown in Fig. 7.

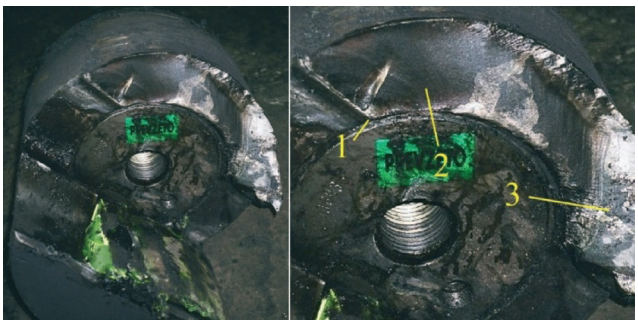

Fig. 7. Fracture of 2nd coupling

A visual examination of the fracture surface of the second coupling showed three fracture regions, Fig.7: the region of fracture origin (at 1), the region of progressive fatigue crack propagation with curved beach marks (at 2), and the final fast fracture zone (at 3). In this case the crack started in the corner of region 1, similar to the previous case but on the opposite paddle. The crack propagated around the corner what is also visible with curved beach marks. The final fracture occured when the region of progressive fatigue crack propagation reached about 65% of the paddle cross seaction. The second fracture origin is not clearly expressed.

The conclusion from the surface investigation was that both couplings fractured as a result of fatigue. The fracture started in the corner between the paddle and the coupling body and propagated around the corner. In both cases the final fracture occurred when the fatigue crack propagation reached about 60-65% of the paddle cross section.

2.2. Stress analysis

2.2.1. Torque of drive shaft

The drive shafts and couplings transmit torque which consists of rolling torque required for deformation and torque required for the friction in the bearings.

The rolling stock passes between two rolls and torque required for deformation is torque of two rolls, Fig.8. The equation for rolling deformation torque, Ref. [3], is given by

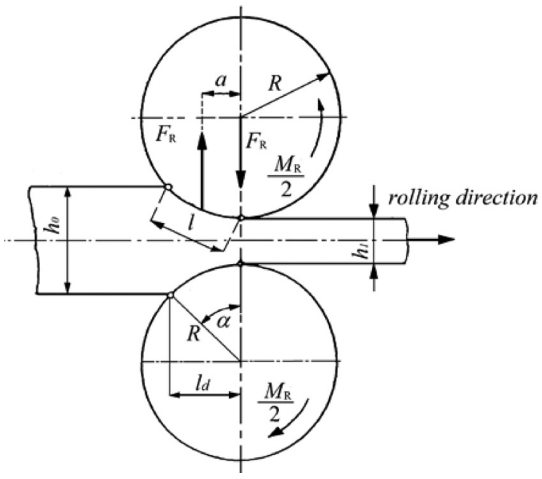

Fig. 8. Rolling force and rolling deformation torque

$$T_R = 2\,F_R \cdot a, \quad (1)$$

where F_R is rolling force and "a" is distance of rolling force from centre of the roll.

The distance of the rolling force from centre of the roll, Ref. [3] and [4], can be calculated as

$$a = 0.5 \cdot l_d \quad (2)$$

where l_d is the projected length of the contact arc.

Each drive shaft transmits half of total rolling torque and torque of drive shaft can be calculated from the rolling deformation torque increased for the friction in the bearing by 10%, Ref. [3];

$$T_{sh} = 0.5 \cdot 1.1 \cdot T_R, \quad (3)$$

where $0.5 \cdot T_R$ is half of rolling deformation torque.

2.2.2. Paddle force

The plastic slippers are installed between the coupling paddles and the driven shaft, Fig.9.

Torque is transmitted through the contact surfaces between shaft and slippers and slippers and paddles. The force acting on each paddle is resultant force of load distributed on the paddle surface from the slipper. The load distribution has trapezoidal shape, Ref. [3]. Drive shaft torque can be expressed, Ref. [3];

$$T_{sh} = F \cdot b, \quad (4)$$

where F is resultant force of distributed load and b is distance between resultant forces, Fig.9.

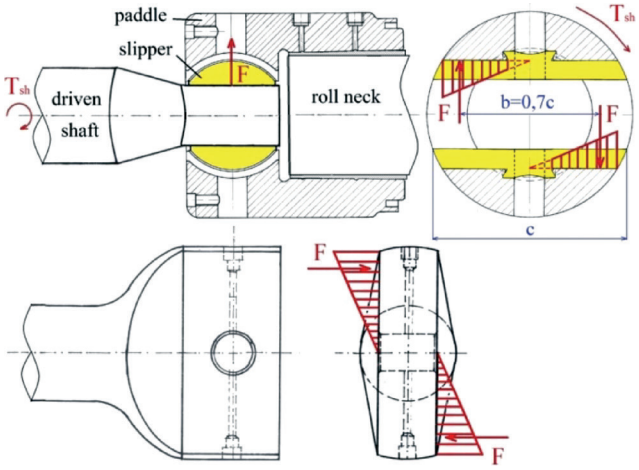

Fig. 9. Coupling load

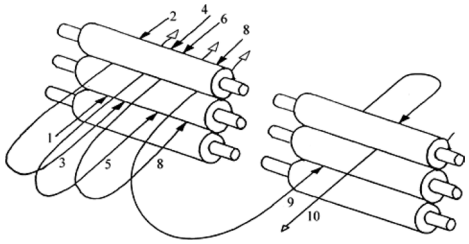

Fig. 10. Roughing mill schema

2.2.3. Torque of middle drive shaft and paddle force change according to time

Rolling in the roughing mill consists of 10 passes in two stands, 8 in the first stand and 2 in the second stand, Fig.10. In each pass a different rolling force acts, Fig.11, and the corresponding rolling deformation torque.

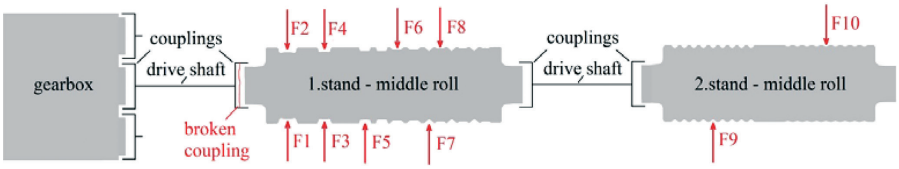

Fig. 11. Roughing mill power transmission

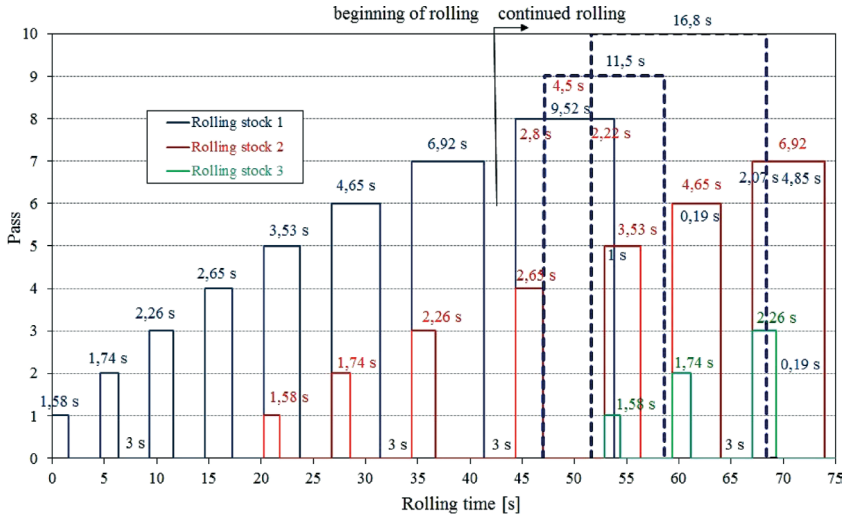

Fig. 12. Roughing mill rolling process

The middle drive shaft between the gearbox and the 1st stand transmits half of the total rolling torque following a rolling sequence of 8 passes in the first stand and 2 passes in the second stand, Fig.12.

The rolling process on the roughing mill begins with the rolling stock in the pass 1 and the rolling time is 1.58 seconds. Between rolling in passes, there is a rolling pause of 3 seconds because of changing the rolling direction. After the rolling pause of 3 seconds, the rolling stock comes in pass 2 and rolling time is 1.74 seconds, followed by rolling in pass 3 and pass 4. After 20 seconds of the first stock start, the rolling of two rolling stocks begins together in passes 1 and 5. The rolling of two rolling stocks together continues in passes 2 and 6, passes 3 and 7 and passes 4 and 8.

Rolling in pass 9 in the second stand starts 2.8 seconds after the first rolling stock goes out from pass 8. Then 4.5 seconds after the rolling starts in pass 9, the first stock comes in pass 10 in the second stand. The rolling of the third stock begins 53 seconds after the first stock starts and the rolling process on the roughing mill continues according to the rolling sequence and repeats until rolling stops.

The rolling process can be divided into two parts; the first part is the beginning of rolling and the second part is continued rolling, Fig.12. In regular service, the first part of the rolling process, rolling beginning, is a very short period of the total rolling in comparison with the second part, continued rolling.

Rolling deformation torque and torque of the middle drive shaft for each separate pass are obtained from Eq. (1), (2) and (3). The paddle force is obtained from Eq. (4). The results are shown in Table 1. The experimentally determined rolling forces were used for the calculation of the drive shaft torque, Ref. [1] and [5].

Table 1. Roughing mill rolling sequence, torque of the middle drive shaft and paddle force

Pass		1	2	3	4	5	6	7	8	9	10
Pass shape		box	box	box	box	box	oval	square	oval	square	oval
Groove dimensions [mm]		100x82	100x66	67x80	67x59	66x52	80x34	40	58x20	30	45x18
Cross-section [mm^2]	9850	8015	6474	5398	4032	3280	2286	1578	1075	890	610
Roll working diameter [mm]		372,5	393,5	372,5	398,5	396,5	419,5	397,25	433	425	441,5
Roll speed [rpm]		120	120	120	120	120	120	120	120	120	120
Length of rolled stock [m]	3	3,69	4,56	5,47	7,33	9,01	12,93	18,73	27,49	33,20	48,44
Projected length of contact arc l_d[mm]		57,84	56,10	72,08	64,68	68,97	61,44	79,10	64,97	56,46	51,47
Rolling time [s]		1,58	1,74	2,26	2,65	3,53	4,65	6,92	9,52	11,5	16,8
Rolling pause [s]		3	3	3	3	3	3	3	3	2,8	4,5
Experimentally determined roll force [kN]		356,1	494,6	356,1	524,2	346,2	544,0	286,8	445,1	180,5	292,2
Distance of force from roll centre *a*[mm]		28,9	28,1	36,0	32,3	34,5	30,7	39,6	32,5	28,2	25,7
Rolling deformation torque [kNm]		10,3	13,9	12,8	17,0	11,9	16,7	11,3	14,5	5,1	7,5
Torque of middle drive shaft [kNm]		**5,7**	**7,6**	**7,1**	**9,3**	**6,6**	**9,2**	**6,2**	**8,0**	**2,8**	**4,1**
Paddle force for separate pass[kN]		**25,3**	**34,1**	**31,5**	**41,6**	**29,3**	**41,0**	**27,9**	**35,5**	**12,5**	**18,5**

The torque of the middle drive shaft change according to time, Fig.13, is constructed from the rolling process on the roughing mill, Fig.12 and the torque of the middle drive shaft for each pass, Table 1.

The diagram in Fig.13 shows that torque change follows the rolling schedule. In pass 1, the torque value was 5.7 kNm with a duration of 1.58 seconds. In pass 2 the torque value was 7.6 kNm with a duration 1.74 seconds.

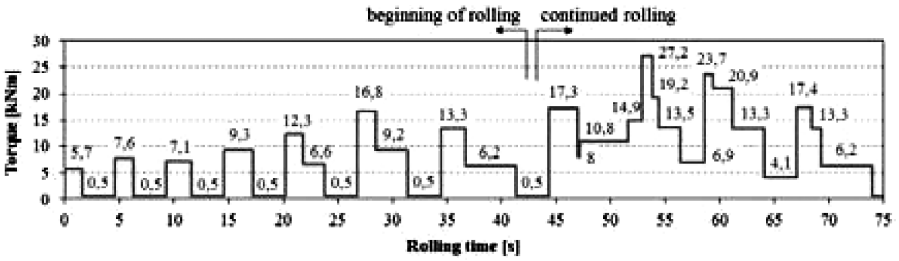

Fig. 13. Drive shaft torque change according to time

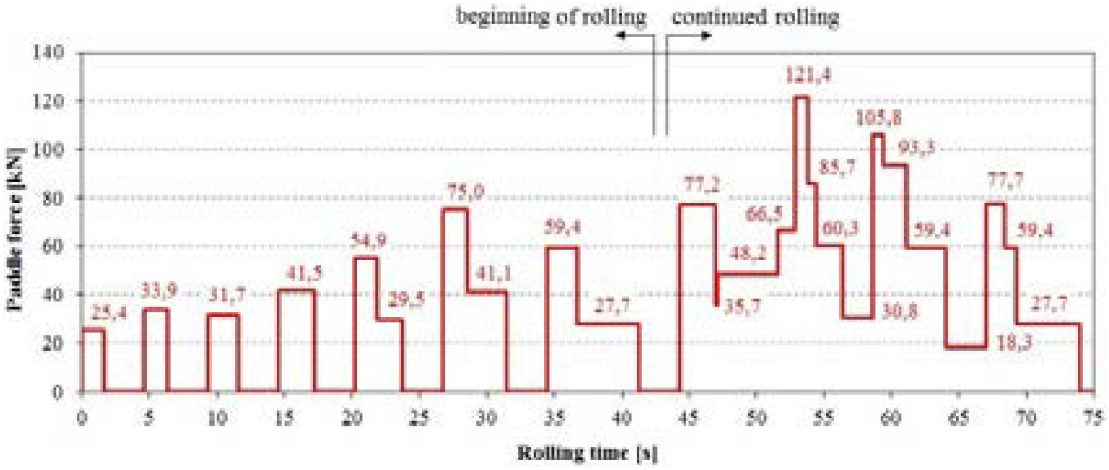

Fig. 14. Paddle force change according to time

In pass 3 the torque value was 7.1 kNm in 2.26 seconds and 9.3 kNm in 2.65 seconds in pass 4. For rolling two stocks in pass 1 and 5 the torque value was 12.3 kNm with a duration of 1.58 seconds, which is a sum of the torque values in passes 1 and 5. Rolling in pass 1 finished after 1.58 seconds, and the torque value was 6.6 kNm with a duration of 295 seconds due to rolling in pass 5.

The paddle force change according to time, Fig.14, was made according to the roughing mill rolling schedule according to time, Fig.12, and paddle force, Table 1.

The diagram in Fig.14 shows that the maximum paddle force was 121.4kN during the rolling of three stocks together in passes 1, 5 and 8, 9 and 10 with a duration of 1 second.

2.2.4. Numerical analysis of the slipper coupling and the drive shaft

The stress analysis of the slipper coupling and the drive shaft was carried out by the finite element method using ADINA software. The linear elastic model with 3D solid elements with eight DOF per nodes was used, Fig.15 and Fig.16. Each node had 3 degrees of freedom, translation in X, Y and Z direction. The model of coupling was fixed in the contact area with the roll and loaded with trapezoidal distributed forces in the nodes on the paddle surface. The model of the drive shaft was fixed in the back side face and loaded with trapezoidal distributed forces in the nodes on the contact surfaces.

FEM analysis of the slipper coupling revealed that a force of 121.4 kN caused the maximum stress of 294

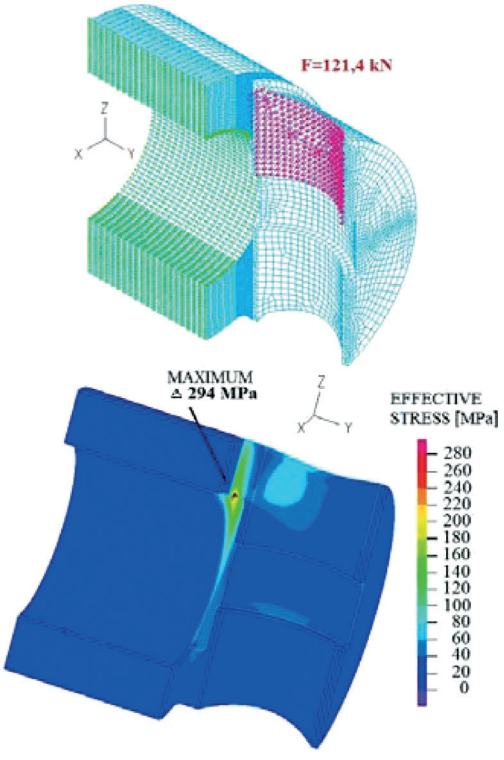

Fig. 15. Numerical analysis of the slipper coupling

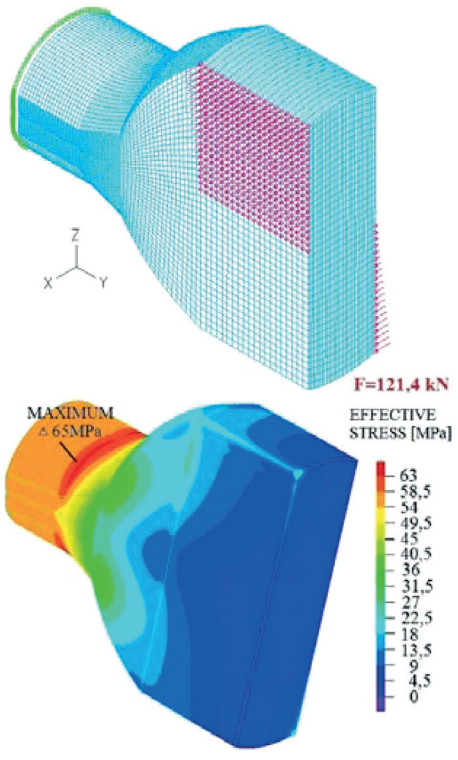

Fig. 16. Numerical analysis of the drive shaft

MPa on the fillet between the paddle and the coupling body, Fig.15, in the same place where both fractures originated. FEM analysis of the drive shaft revealed that the maximum stress of 65 MPa appeared due to change in the shaft diameter, Fig.16, and that the drive shaft was not the critical point.

3. Proposed design modifications

The analysis showed that both fractures were caused by the deficient design of the fillet between the paddle and the coupling body with high stress concentration. In order to extend the actual service life, three design modifications were considered:

a) Decreasing the stress concentration in the corner between the paddles and the coupling body by change of the fillet radius and the grove radius, Fig.17a;

b) Increasing the external diameter of the coupling in the critical place, Fig. 17b and

c) Redesign of the coupling with stiffener between the paddle and the coupling body, Fig. 17c.

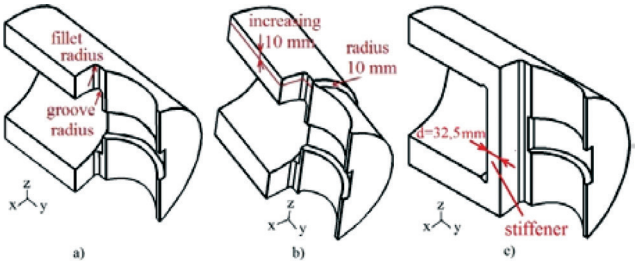

Fig. 17. Considered actions

In the first and the second solution the redesign was limited only to reshape the coupling and did not request any change of the shaft. The third solution involved also redesigning the shaft – reducing the shaft length by 100 mm.

3.1. Change of fillet and groove radius

The high stress concentration is caused by two stress raisers, the fillet and the groove in the corner between the paddle and the coupling body. The change of the fillet and groove radius was analyzed in order to reduce stress concentration. The radius of the fillet was limited by the free space necessary to move the shaft the coupling and can be increased from 8.5 mm to 10 mm, Fig.18. The radius of the groove was controlled by the groove width and the groove width could not be increased, Fig.18.

FEM analysis of local stresses revealed that a redesign by changing the radius of the fillet will slightly decrease local stresses.

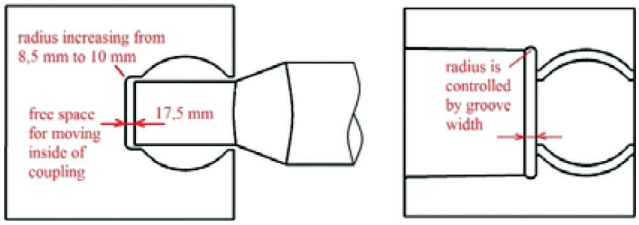

Fig. 18. The space between the shaft and the coupling

3.2. Increasing the external diameter of the coupling in the critical place

The rolls during exploitation reduce the working diameter by turning due to roll wearing. The gap between the rolls should be adjusted in the requested dimension by reducing the distance between the roll axes. Because of that, the minimum of the free space between the external diameters of two couplings was 80 mm, Fig. 19, which allowed increasing the external diameter of the coupling from 340 to 360 mm. Additional increasing the external diameter may disturb the assembly and maintenance work.

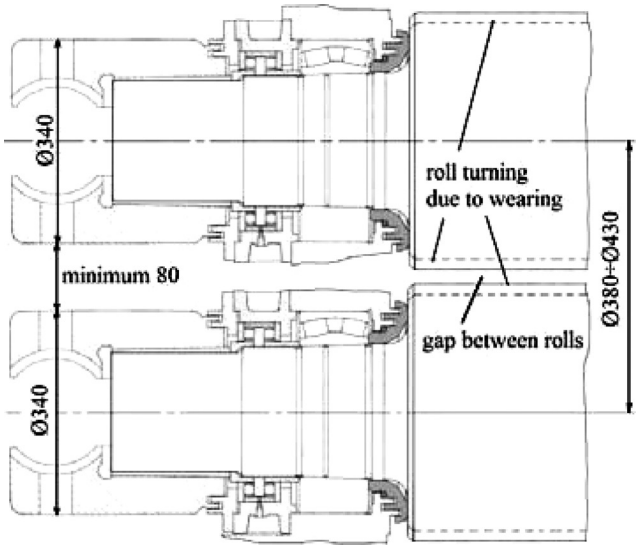

Fig. 19. Space between the external diameters of two couplings

FEM analysis of local stresses revealed that increasing the external diameter from 340 mm to 360 mm reduced the maximum local stress from 294 MPa to 251 MPa, Fig. 20.

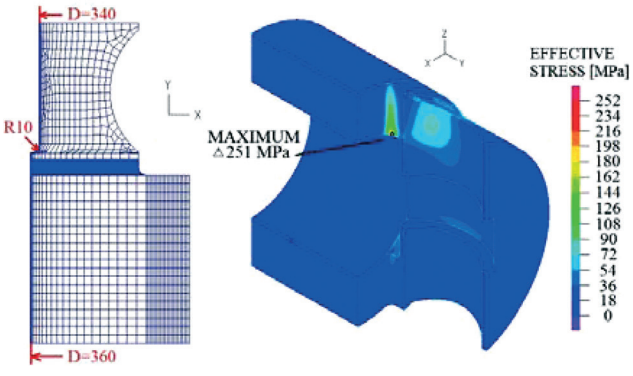

Fig. 20. FEM analysis with the increased external diameter

3.3. Redesign of the coupling with stiffener between the paddle and the coupling body

In the original design there was an interference of two stress raisers, the fillet and the groove. The redesign of the coupling with stiffener between the paddle and the coupling body was considered in order to split influences of stress raisers on local stresses. A numerical analysis of local stresses was carried out for the new design with a stiffener thickness of 12.5 mm and 32.5 mm, Fig. 21. With the new design, the distance between the fillet centre and the groove centre with a stiffener thickness of 12.5 mm was 30 mm and with 32.5 mm it was 50 mm.

FEM analysis revealed that the redesign of the coupling with a stiffener thickness of 12.5 mm reduced the maximum local stress from 294 MPa to 163 MPa (about 44%) and with a stiffener thickness of 32.5 mm it was reduced from 294 MPa to 139 MPa (about 52%).

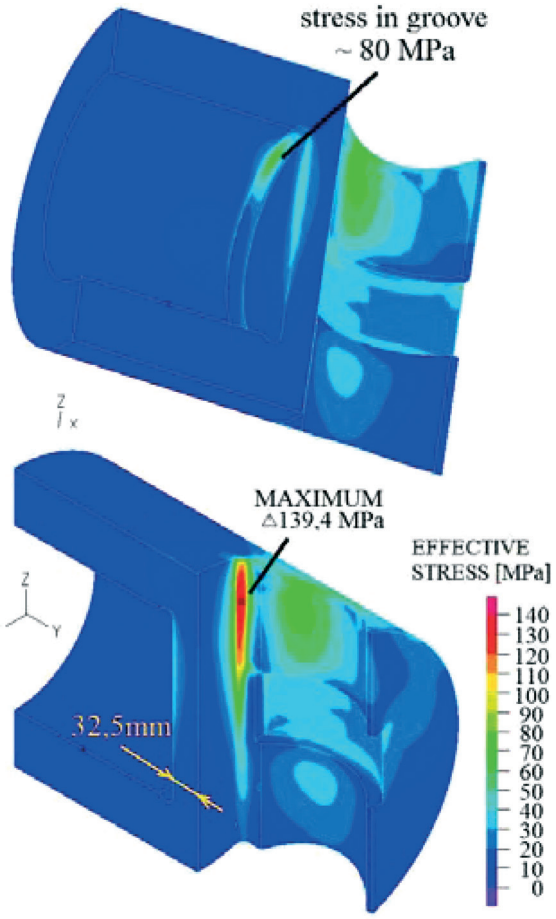

Fig. 21. FEM analysis of the new coupling design with a stiffener thickness of 32.5 mm

3.4. Service life

The actual service life of couplings was estimated from the mill production and rolling schedule. The service life of the couplings was divided into the sequences depending on roll wearing. The roll service life before machining due to wearing was estimated after 4000 rolling tons of steel (about 15 working days or about 17390 rolled billets). After that period, the rolls should be replaced and machined on new working dimensions. The couplings should be dismantled and installed again after the roll machining.

Each sequence of coupling service life was also about 4000 rolling tons. During continued rolling, the drive shaft torque for one billet changed 15 times, Fig. 13. For 17390 billets the total number of the drive shaft torque changed about 260000. During one sequence of the coupling service life the maximum drive shaft torque was 17390, so the number of cycles of maximum stress was also 17390.

Based on this data, the actual service life of the coupling was estimated for 27 working sequences, (469530 divided by 17390 is 27), or 405 working days (time period about 3 years), Fig. 22. The fatigue strength curve of the

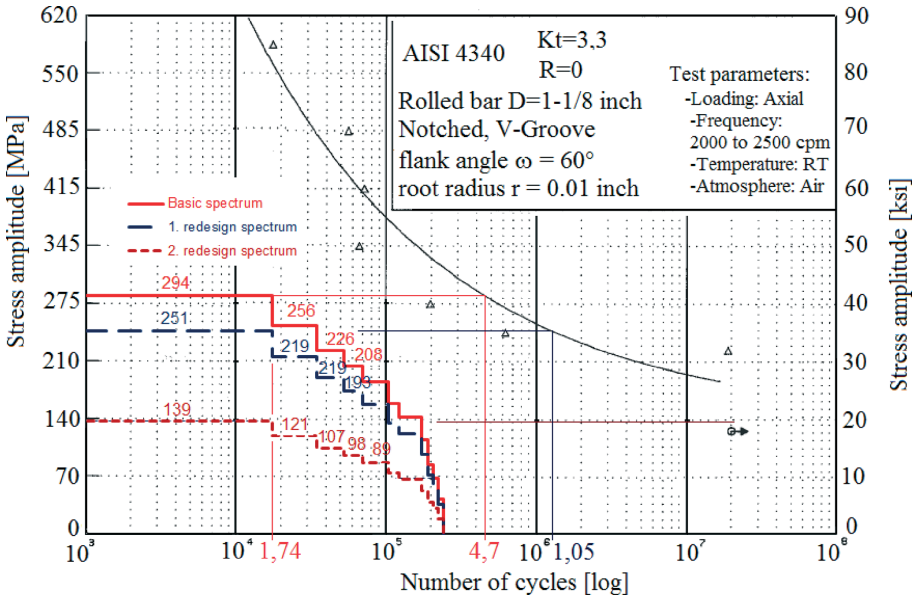

Fig. 22. Stress spectra for critical area

material was used from literature [8] for the equivalent material 4340 according to ASTM (American Society for Testing and Materials) [9].

The redesign by increasing the external diameter of the coupling in the critical place reduced the maximum local stress by about 15% (from 294 MPa to 251MPa) and increased fatigue life by about 100% according to the actual estimated fatigue life, Figure 22.

The redesign of the coupling with a stiffener between the paddle and the coupling body reduced the maximum local stress below the fatigue endurance limit (from 294 MPa to 139 MPa).

Based on this analysis, the actual service life of the shaft can be improved from the finite (about $4.7 \cdot 10^5$ cycles) to the infinite lifetime.

4. Conclusion

The failure analysis of two slipper couplings showed that both couplings fractured as a result of fatigue due to a deficient design. In both cases, a fracture started in the corner between the paddle and the coupling body, and propagated around the corner. The final fracture occurred when the fatigue crack propagation reached about 60-65% of the paddle. In the basic design, the corner between the paddle and the coupling body was the intersection of two stress raisers, the fillet and the groove.

Three design modifications were considered to avoid having high stress concentration at the corner between the paddle and the coupling body. In the first solution, numerical analysis of local stresses revealed that a redesign by changing the radius of the fillet and the radius of the groove will not reduce local stresses because of the interference of two stress raisers. In the second solution, numerical analysis of local stresses revealed that an increase in the external diameter from 340 mm to 360 mm reduced the maximum local stress by about 15% and increased fatigue life by about 100% according to the actual estimated fatigue life. In the third solution, numerical analysis showed that a redesign of the coupling with a stiffener between the paddle and the coupling body reduced the maximum local stress and the actual service life of the couplings could be improved from the finite to the infinite lifetime.

Taking relatively a simple corrective measure of the design, such as the last one described, will greatly improve component reliability and prolong the life of components, reducing overall costs. New couplings were made by redesigning the coupling with stiffener between the paddle and the coupling body to prevent recurrence of the failure.

References

[1] Ž. Domazet, F. Lukša, M. Šušnjar. Failure analysis of rolls with grooves. Engineering Failure Analysis, Volume 14, Issues 6; September 2007, pages 1116-1174

[2] Deutsches Institut für Normung. DIN 17200. 1987 (DIN, Berlin)

[3] M. Čaušević. Obrada metala valjanjem. Veselin Masleša; Sarajevo 1983.

[4] J. Hribar. Plastična obrada metala. FSB; Zagreb 1975.

[5] Ž. Domazet, F. Lukša. Experimental determination of the rolling force on the rolls with grooves. Proceedings of the 22-nd Symposium "DANUBIA-ADRIA" on Experimental Methods in Solid Mechanics; Parma 2005.

[6] F. Lukša. Investigation of the cause of the failures of the rolls with grooves. Master Thesis, University of Split, Faculty of Electrical Engineering, Mechanical Engineering and Naval Architecture. Split 2005.

[7] Designs and technological rules "Steelworks Split". Split

[8] Metallic Materials and Elements for Aerospace Vehicle Structures. MIL-HDBK-5B, Military, Standardization Handbook. U.S. Department of Defense, 1987

[9] American Society for Testing and Materials. ASTM 322-A91. ASTM International, 2001

Engineering Power – *Bulletin of the Croatian Academy of Engineering* Vol. 15(1) 2020 – ISSN 1331-7210

Publisher: Croatian Academy of Engineering (HATZ), 28 Kačić Street, P.O. Box 59, HR-10001 Zagreb, Republic of Croatia

Editor-in-Chief: Prof. Vladimir Andročec, Ph.D., President of the Academy retired Full Professor with tenure, University of Zagreb, Faculty of Civil Engineering

Editor: Prof. Zdravko Terze, Ph.D., Vice-President of the Academy University of Zagreb, Faculty of Mechanical Engineering and Naval Architecture

Guest-Editor: Željko Domazet, University of Split, Faculty of Electrical Engineering, Mechanical Engineering and Naval Architecture

Editorial Board: Prof. Vladimir Andročec, Ph.D., Prof. Zdravko Terze, Ph.D., Prof. Slavko Krajcar, Ph.D.

Editorial Board Address: Croatian Academy of Engineering (HATZ), "Engineering Power" – Bulletin of the Croatian Academy of Engineering, Editorial Board, 28 Kačić Street, P.O. Box 59, HR-10001 Zagreb, Republic of Croatia

E-mail: hatz@hatz.hr

Graphical and Technical Editor: Vladimir Pavlić, Dipl. Eng. (Riječ i slika, Zagreb) *Press:* Tiskara Zelina, Ltd., Zelina

Circulation: 200